

# Variability of Southern T Tauri Stars I: The Continuum and the $H\beta$ Inverse PCygni Profile of GQ LUPI

C. Batalha, D.F. Lopes and N.M. Batalha<sup>2</sup>

## ABSTRACT

We present time series spectrophotometric observations of GQ Lupi, a typical representative of the YY Ori subgroup of T Tauri stars that show conspicuous inverse PCygni profiles. The data set consists of 32 exposures taken over 5 and 8 consecutive nights of May and July 1998, respectively, and covers the spectral range of  $3100 \text{ \AA} < \lambda < 5100 \text{ \AA}$ . The region redward and next to the Balmer jump varies significantly on a night-to-night basis and the amplitude of such variability decreases sharply at  $\lambda > 4600 \text{ \AA}$ . The Balmer continuum slope indicates that the spectral energy distribution is governed by a gas of temperature greater than that of the stellar photosphere. The variability of the Balmer continuum flux has the largest amplitude. Flux increases in the B band are accompanied by concurrent flux increases in the U band. The contrary is not always verified.

The excess of continuum emission (veiling) for each exposure is computed throughout the spectral format. We find a tight anticorrelation between the veiling and the observed Balmer jump. We report the largest inverse PCygni profile ever observed at this resolution: the depth of the  $H\beta$  absorption component is nearly twice the height of the peak emission. Surprisingly, this absorption vanishes a few nights later. The time series of the redward absorption component behaves similarly to the veiling time series: the progressive weakening of the redward absorption is closely followed by a similar weakening of the excess continuum emission. If the absorption component is de-veiled, the correlation strengthens. Thus, large/small redward absorption = large/small veiling = small/large Balmer jump.

We model the emitting region by a gas of uniform temperature and density: each of the 32 exposures acting as a snapshot of such a region for a given stellar rotational phase. We explore models of temperature greater than 5000 K and number of hydrogen atoms ( $N_H$ ) larger than  $10^{13} \text{ cm}^{-3}$ , extending the gas spectral energy distribution up to the blackbody of a given temperature. The resulting models indicate that the gas densities and the respective temperatures are strongly anticorrelated. In addition, the model time series show that the increase in the gas density is mirrored by an increase of the projected emitting area (filling factor). Large/small gas densities and filling factors are characterized

by high/low observed veiling. As the accretion rate fades from night-to-night, the observed veiling decreases, as does the gas density and the total projected emitting area.

*Subject headings:* Accretion, accretion disks – stars: T Tauri, pre Main Sequence  
– stars: YY Ori, individual (GQ Lupi)

## 1. Introduction

According to current models of classical T Tauri stars (CTTS), the steady migration of the gas in a circumstellar accretion disk is suddenly halted at a few stellar radii by the stellar magnetic field (Uchida & Shibata 1984; Camenzind 1990; Königl 1991, Shu et al. 1994). Material then free-falls onto the star, guided by stellar magnetic field lines. If an axisymmetric bipolar configuration of the stellar magnetosphere is further invoked, the circumstellar gas – which is confined near the equatorial orbital plane – will end its collapsing trip on high latitude stellar regions. This scenario explains the small projected rotational velocity ( $v \sin i < 15 \text{ km s}^{-1}$ ) found among CTTS. The field lines, crossing the circumstellar disk beyond the co-rotational radius, meet the disk atmosphere rotating more slowly than the stellar surface thereby braking the star and regulating the stellar angular momentum during the early phases of stellar evolution (Bouvier et al. 1993; Edwards et al. 1993). A natural consequence of such a paradigm is the occurrence of absorption features in the red wings of the broad emission lines commonly observed in CTTS. An inverse PCygni profile (IPC) will result in those cases where a red-shifted absorption component depletes the local continuum.

The inverse PCygni profiles were highlighted for the first time in pre–Main Sequence studies by Walker (1972). He detected IPC in the high Balmer lines of the star YY Orionis, dubbing a new sub–class of pre–Main Sequence objects after this star. The presence of the IPC in YY Ori stars was interpreted as the result of quasi–radial accretion operating during the very final stages of the protostellar hydrodynamic evolution (Walker 1972; Appenzeller & Wolf 1977). This view was discarded after the discovery of a handful of CTTS which display lines with normal PCygni profiles – indicative of mass outflow – as well as lines with inverse PCygni profiles, indicating mass infall. Occasionally, they would change from one to the other on time scales of days (Krautter & Bastian 1980). Thus, a more complex mass motion incorporating gas flow in nearly opposite directions had to be developed. Mundt (1984) suggests that material is falling back onto the star after being ejected at velocities smaller than the escape velocity. Mass transfer from a secondary onto the YY Ori star is

also discussed in Grasdalen (1977). More recently, Edwards et al. (1994), analyzing high resolution spectra of 15 CTTS with a broad range of accretion rates, concludes that the large majority of these objects displays redshifted absorption or profile asymmetries indicative of mass infall. Thus, rather than being an exception to the rule, the YY Ori features are actually common properties of CTTS.

Bertout et al. (1982) reports on high resolution spectroscopy of two bright YY Ori stars during 12 consecutive nights – GQ Lupi being one of them. They find that the redshifted absorption component shows the largest variability on a short time scale compared to the other line components. These findings were reinforced by Aiad et al. (1984) who conducted a temporal survey of a few YY Ori members. They find that the time scale for the redshifted absorption variability depends on the star and that these features are formed in a free-falling matter within a few stellar radii. With velocities larger than a few hundreds of kilometers per second, and subject to short term variability, the IPC stands as a tracer of accretion mediated by magnetic field lines (Aiad et al. 1984). Lehmann, Reipurth & Brander (1995) observed EX Lupi during a maximum in emission and a few months later when the star had dimmed. The IPC is only present during the bright phase. They interpret this outburst in terms of an increase of mass accretion, with the consequent increase in the continuum flux and the spectral veiling. At maximum continuum emission, the photospheric lines vanish and IPC’s are clearly visible.

Line emission is also thought to be produced in the accretion funnel (Calvet & Hartmann 1992) rather than in pure winds (Mundt 1984; Hartmann et al. 1990). Hartmann, Hewett & Calvet (1994) develop infall models with a dipole configuration for the magnetic field geometry. They restore most of the Balmer line features seen in CTTS such as the lack of redshifted absorption in the H $\alpha$  line compared to the higher Balmer lines and the slightly blueshifted emission peak of the Balmer lines. However, Johns & Basri (1995a) note that the nearly symmetric profile and the full width at zero level of the average H $\alpha$  emission of SU Aur cannot be reproduced in an accretion funnel alone. Instead, they claim that the bulk H $\alpha$  emission is produced in an almost stationary zone close to the star and that turbulence, not the velocity field, broadens the line.

Time series analysis is extremely suitable for exploring the circumstellar gas configuration for this class of objects. A single snapshot, at any spectral resolution, allows, at the most, a short glance at an intricate gas flow. On the contrary, time series analysis allows for the search of correlations among selected components of line profiles, among several line groups, and between line and continuum fluxes of a given star (Bertout et al. 1982; Giampapa et al. 1993; Johns & Basri 1995a,b; Petrov et al. 1996; Gullbring et al. 1996; Johns & Basri 1997; Hessman & Guenther 1997; Lago & Gameiro 1998). SU Aur has been

a common target for such analyses (Giampapa et al. 1993; Johns & Basri 1995; Petrov et al. 1996). Its  $H\alpha$  line profile has a blueshifted absorption feature with periodic behavior. A similar feature is also found in the  $H\beta$  line, together with an absorption feature on the red side of the profile. Both features modulate with the stellar rotation and are nicely explained within the framework of the X-celerator model of Shu et al. (1994 – see also Johns & Basri 1995a).

The large majority of projects taking advantage of time series observations use high resolution data. Thus, with unprecedented detail, information regarding the gas configuration of the regions contributing to each individual feature of the line profile is consistently recovered. The intrinsic limitations are to obtain a sufficient number of nights to secure the completion of the goals and to have enough signal to recover the photospheric absorption lines which are crucial for determining veiling.

We initiate a project based on time series observations of CTTS, aiming to collect spectrophotometric and high resolution data of “VARIability of Southern T Tauri Stars” (VASTT, henceforth). The main goal is to monitor the spectral line variability and the continuum changes as a means of improving our understanding of their surrounding circumstellar gas. We attempt to recover flux-calibrated observations, weather allowing. When unfeasible, we attempt to recover at least the shape of the spectral energy distribution after observing photometric standards throughout the night. In this contribution we determine the evolution of the  $H\beta$  line emission component, its redshifted absorption component and the spectral veiling for the star GQ Lupi, which is a well known representative of the YY Ori sub-class.

## 2. Observations

The data presented in this communication are part of a larger data set of CTTS observed during 6 and 8 consecutive nights of May and July 1998, respectively. The stars were selected from the brightest members of the Cha and Lupus complexes and a detailed study of each will be presented in forthcoming papers.

The  $EW_{H\alpha}$  of GQ Lupi is  $2.8 \text{ \AA}$  (Herbig & Bell 1988) which is certainly not typical for a CTTS. The “Pico dos Dias Survey” (PDS) indicates a somewhat larger  $H\alpha$  equivalent width of  $86 \text{ \AA}$  (C.A.O.Torres – private communication). The classification of GQ Lupi as a member of the YY Ori sub-class together with its reported variability led us to include this star in our survey of CTTS. However, the motivation for tackling the GQ Lupi data set first is based on the appearance of inverse PCygni profiles seen conspicuously in the high Balmer line members up to  $H\beta$  and the CaII H and K lines (see Figure 1 in JD = 2450942.925). The

IPC signatures vanish a few days later (see Figure 1 in JD = 2450947.900) with the Balmer lines and the Balmer discontinuity presenting their largest emission. Two months later, our second observing run caught the strongest absorption of an IPC ever reported at our resolution, with the  $H\beta$  line indicating no more than a modest peak of emission (see Figure 1 in JD = 2450997.752). July observations show smoothly varying line strengths. Other CTTS showed inverse PCygni profiles during our campaign but neither their variability nor their strength matches that of GQ Lupi.

GQ Lupi inverse PCygni profiles have been reported previously by Bertout et al. (1982) who assign to this feature the highest variability among all other line features. It is listed as a K7 V star, with  $EW_{H\alpha} = 2.8$  (Herbig & Bell 1988).

## 2.1. Instrumentation and Data Reduction

Spectroscopic observations were collected with the ESO 1.52m telescope at La Silla with the Boller & Chivens spectrograph. Spectral windows extend from 5200 Å down to 3100 Å, which includes the major spectral features directly responsible for the strong U and B modulation reported for TTS. Gratings are chosen to maximize the response (# 31 and 33) at these wavelengths. Having in mind that precise veiling measurements are an important aspect of this program, we aim for a S/N larger than 100 during clear nights. An integration time of 10 - 15 minutes for a star of  $V = 12$  was typically employed. The spectrograph feeds a Loral Lesser CCD instrument (2048 x 2048) providing an effective resolution of 2 Å. The slit was open to 5 arcsec to include the whole seeing disk. Some of the stars were monitored several times a night (GQ Lupi included) and large zenith angles were likely to occur. Thus, the slit orientation was moved to a new position angle in order to correct for differential refraction and minimize the light losses. The corrections rely on the curves presented by Filippenko (1982). Table 1 presents the observation logs. Observers on preceding and proceeding nights joined efforts to monitor the GQ Lupi spectral variability. The instrumental settings were not necessarily the same but they allow a few overlapping spectral windows, such as that including  $H\beta$ . This supplementary data will be reported in another communication.

Fig. 1.— Spectrophotometric observations of GQ Lupi for the May and July (1998) runs. Only exposures representative of each observing night are presented. Conspicuous inverse PCygni profiles (IPC) are seen in some of the exposures, especially at JD = 2450997.752. Significant line emission is detected at JD = 2450947.900, with no indication of inverse PCygni absorption component.

The data is reduced in a standard way, with flat-fielding, bias and sky subtraction, using IDL-based routines developed by G. Basri (private communication). Due to the flexing of the optical system at different telescope positions, a calibration lamp (He–Ar) is taken after each series of observations targeting a group of closely spaced stars. We identify an average of 30 lines with a 5<sup>th</sup> order polynomial fit, yielding an accuracy of about 15 km s<sup>-1</sup> in the dispersion solution.

## 2.2. The Flux Calibrations

Two spectrophotometric standards (Hamuy et al. 1992) were observed throughout the night and used as flux calibrators (EG 274, LTT 7379). Essentially, we observed rounds of 5 to 10 TTS and then the standards, thus assuring a series of response curves for each night distributed over different air masses. The nights were not photometric, prohibiting an accurate determination of the extinction law and subsequent flux calibrations. Consequently, stellar radius cannot be derived in a self consistent way. During the 1999 observing run, whose analysis will be presented in a forthcoming communication, we observed GQ Lupi for nearly 20 consecutive nights and under ideal conditions, which will permit us to access its basic stellar parameters.

We adopt the May and July (1997) average extinction coefficients of La Silla, kindly provided by the Geneva Observatory Photometric Group. Variable atmospheric transmission on a daily or yearly basis will change the absolute value of the adopted coefficients – which are wavelength dependent – thereby affecting the final spectral energy distribution (SED) of the star. After inspecting the night to night variability of the Geneva coefficients, we estimate these errors to be less than 2 %, which are negligible when compared to the intrinsic stellar variability.

Wavelength independent flux shifts are likely to be incorporated into the nightly set of sensitivity functions (SF) due to cloud transit. To monitor the shape changes of the TTS spectral distribution - which is one of our goals - one needs to estimate the instrumental signature of the night. The whole set of response curves are moved to the brightest, which is assumed to be taken under the best sky conditions. Thus, the residuals among the response curves are minimized after gray shifting each curve to their new average. The absolute flux error due to cloud transit is the difference between the dimmest and the brightest response curve and can be found in Table 1. The internal error of the shifted SF's around the median is usually less than 4% for  $3400 \text{ \AA} < \lambda < 5000 \text{ \AA}$  and rises steadily outside this region. At wavelengths  $< 3400 \text{ \AA}$ , the signal diminishes due to a drop in the atmospheric transmission which leads to a poorly defined spectral light distribution. We list in Table 1 the absolute

flux uncertainties due to variable atmospheric transparency.

A subset of the observations, with representative spectra of each of the observing nights, is displayed in Figure 1 with their corresponding Julian dates. Light losses were registered at  $\text{JD} = 2450944.687$  and  $2450945.826$ , especially in the blue, due to the transit of cirrus, severe winds, and the consequent effect on the tracking. The corresponding SED’s are therefore unreliable.

### 3. Results

Detailed identifications of the emission lines present in the GQ Lupi spectrum are presented in Appenzeller, Mundt & Wolf (1977) and Bertout et al. (1982). It is possible to infer from the Bertout et al. (1982) data that this CTTS has moderate levels of continuum excess. The photospheric absorption lines are well discerned even in the blue part of the spectrum where the continuum excess is more severe. It is true that the veiling is better determined with high resolution observations. However, this particular spectral format offers several deep lines which can yield average veiling values over  $50 \text{ \AA}$  windows (see below).

The Balmer emission lines – markers of disk accretion (Valenti, Basri & Johns 1993 – VBJ henceforth) – plus the H & K CaII lines are the only consistent emission lines throughout the observing run. The helium line  $\lambda 4471$  and perhaps  $\lambda 4026$  are also marginally present. On the last night of the May run, the Balmer emission increases severely and the Fe II lines  $\lambda\lambda 4923$  and  $5018$  appear.

#### 3.1. The Time Series of the Spectral Continuum Distribution

The variable transparency over the course of the observing run is a hindrance to directly measuring the SED. We therefore investigate the evolution of flux ratios instead, assuming achromatic flux shifts cancel out. Spectral windows representative of the local continuum are defined for each of the observations which are then normalized by the flux,  $F_{4970}$ .

Fig. 2.— Spectral windows clear of emission lines are selected for determining the Balmer and the Paschen continuum slopes. Each spectrum is normalized at  $4970 \text{ \AA}$ , and an offset equal to the time lag between consecutive exposures is added for display. Light losses were registered for the observations plotted with dot-dash lines.

### 3.1.1. The Balmer Jump

The Balmer jump of several CTTS has been previously measured and compared with other properties of the gas flow (VBJ, Gullbring et al. 1988 – GHBC, Calvet & Gullbring 1998 – CG). These works bring together single observations of a variety of CTTS while this study investigates the evolution of the Balmer jump for a single star. VBJ and CG compute the Balmer jump by modeling the excess emission flux (de-reddening the observed SED and subtracting out the spectral distribution of the underlying photosphere). We take a slightly different approach, quantifying the Balmer jump directly from the observed SED. More specifically, the Balmer jump is defined to be the ratio between the fluxes blueward and redward of the nominal discontinuity. We assign 10 points that are far from major emission lines or strong absorption lines to determine where the local continuum is. The closest *continuum* window redward of the Balmer jump is at 3860 Å, 200 Å off the nominal Balmer edge. The spectra are normalized to the continuum flux window at 4970 Å, and a constant equal to the time lag between observations is added to these normalized spectra for presentation in Figure 2. Light losses were registered during two of the exposures and the corresponding SED should be analyzed with caution (see the dot-dash data of Figure 2).

The spectral distribution changes clearly on a night-to-night basis. In particular, variability is noted at frequencies near the Balmer discontinuity.

Figure 3 illustrates the evolution of the flux ratio across the Balmer jump ( $\lambda F_{\lambda < 3640} / \lambda F_{\lambda > 3640}$ ). Open circles indicate the data subjected to light losses. Measurement of the Balmer jump is subject to various systematic errors. The unresolved forest of blended emission lines (H and CaII) prevents a clear definition of where the continuum should rest. The situation is also problematic when there is significant absorption in the inverse PCygni profiles, especially those near the Balmer discontinuity. The nightly response curves are uncertain for wavelengths shorter than 3400 Å. Therefore, only 200 Å is effectively used to identify the Balmer continuum slope. On the other side of the jump, 200 Å separates the last well-identified (Paschen) continuum window from the edge of the jump, reducing the precision of a polynomial extrapolation. The continuum window at 3860 Å is abandoned in the extrapolation procedure due to the presence of the CN band. Thus, we make linear extrapolations of the closest continuum windows (two in the Balmer and four in the Paschen continuum) towards the jump. The extrapolated Balmer continuum flux deviates by less than 2 % of the observed flux near the edge, increasing to 5% in the spectra of lowest S/N. Assuming a similar uncertainty in the projected Paschen continuum flux towards the jump, the estimated error of the Balmer jump flux ratio is less than 10% (two-sigma error bars are used in Figure 3).

Fig. 3.— The Balmer jump time series is shown for the May and July runs. The Balmer



jump is defined in section 3.1.1 as the flux ratio between the extrapolated Balmer and Paschen continua towards the jump. It shows smooth variability, with local maxima at  $\text{JD} = 2450947.911$  and  $2451003.473$ .

Fig. 4.— The GQ Lupi time series reveals large emission on the night beginning at  $\text{JD} = 2450947.607$ . The Paschen continuum excess does not change significantly while the Balmer continuum excess does (solid line). At  $\text{JD} = 2450997.511$ , the Balmer jump is minimum (dots).

Fig. 5.— **a)** The Balmer continuum slope time series as a function of the Balmer jump. Arrows indicate the time progression for the July series. **b)** The same as **a)**, for the Paschen continuum slope. . The data subjected to light loses are shown as crosses.

During the last night of the May run (May 14, 1998), the Balmer continuum brightens while the Paschen continuum maintains its shape and strength. This can be seen in Figure 4 where each spectrum is shown with solid lines. Contrastingly, the Balmer jumps of  $\text{JD} = 2450997.752$  decrease to a minimum, the Balmer slope being nearly a continuation of the Paschen continuum towards shorter wavelengths. This is illustrated in the same Figure as dots. We note the excess in the B band seen in the curve of  $\text{JD} = 2450997.752$  (broken line), which will be further explained (see Figure 6 below) as a direct result of different veiling distributions. In this exposure, the Balmer emission lines show the largest inverse PCygni profiles ever observed in GQ Lupi, perhaps in any classical TTS (see Section 3.3.1). Furthermore, sharp U-band variations on the last night of May are also depicted in Figure 4. We closed the May run with GQ Lupi showing a very large Balmer jump and opened the July season with nearly no Balmer jump. It then evolves towards values larger than 2.0, increasing and then fading on the last two nights.

It is important to emphasize, in regards to Figure 4, that the brightening of the Balmer emission is not followed by a concurrent change in the shape or strength of the Paschen continuum (see the next section on the measured veiling). It suggests that the brightening of the Balmer continuum comes from a region that is physically more extended or not directly associated with that of the Paschen continuum. Density and/or temperature changes in the emitting region might also cause similar behavior.

The evolution of the Balmer jump depends on the evolution of the Balmer and the Paschen continuum slopes. In Figure 5 **a,b** we correlate the Balmer jump with the slopes of the Balmer and Paschen continua respectively. Open circles are used for the May observations. The reduced number of observations in May precludes us from inferring any obvious evolutionary trend in the slopes for this month. Arrows are included in both panels to indicate the time progression of the exposures. First, we note that the Balmer jump is

correlated with both the Balmer and Paschen continuum slopes (linear Pearson coefficients of -0.73 and 0.85 are computed for the Balmer and Paschen slopes respectively). This is expected if the forming regions have a common energy source providing the emission. Second, both slopes start out as if the temperature of the emitting region was progressively growing. If no excess emission is present, the slopes should reflect those of a cool photosphere peaking at red wavelengths. The progression of the slopes indicate the brightening of the emission region. The temperature increase shows cadence with the size of the Balmer jump (ordinate). However, the trend can also be explained by combining different sizes of emitting areas, gas temperature and opacity (the slab model scenario) or by advocating distinct emitting regions for the Balmer and the Paschen continuum (the shock model scenario (CG)). This trend is reversed at JD = 2451003.473, when the Balmer jump starts decreasing as the blue excess increases. Figure 5 **a** and **b** also indicates that the Balmer continuum slope throughout the season changes less (0.2) than that of the Paschen continuum (0.5).

These changes are, in fact, artifacts of the spectral veiling distribution (Hartigan et al. 1988; Basri & Batalha 1990; Hartigan et al. 1991) which can be consistently measured in GQ Lupi.

### 3.1.2. *The Veiling Time Series*

Several absorption lines are present in this spectral format and are well distributed over the region of the Paschen and the Balmer continua. They are used in previous calculations of VBJ and GHBC to recover veiling in a large sample of TTS, observed with similar spectral format. The CaI line at 4226 Å is one of the strongest absorption lines in the Paschen continuum region, followed by a family of strong iron lines at  $\lambda > 4800$  and a TiO band at 4750 Å, not always strong in the GQ Lupi time series. The lines blueward of the Balmer jump suffer from being in a region of lower S/N due to a combination of decreasing instrumental response and less stellar flux. Nevertheless, a strong blend (at our resolution) of several iron lines of low excitation potential at 3550 Å is clearly seen in most of the data, allowing us to extend the *veiling distribution*, as a function of time, to this region. The star Gliese 825 (K7 V) is the template for the de-veiling procedure.

We divide the spectrum into windows of 50 Å and assume that the excess of continuum external to the photosphere ( $F_{ext}$ ) is flat within this window ( $F_{ext}/F_{phot} = const$ ). This is supported by previous measurements of TTS veiling taken with data of higher S/N (Stout–Batalha, Batalha & Basri 2000; Hartigan et al. 1991; Basri & Batalha 1990). The spectra of the TTS and the template are normalized over a larger spectral region (150 Å) in order to decrease the uncertainties regarding the continuum placement. Then, a first guess to

the average veiling is obtained by minimizing the  $\chi^2$  of the model fit (the veiled template) applied over the entire 150 Å window. This is followed by fine adjustments (steps of 0.1 in veiling). We estimate veiling measures with errors less than  $\pm 0.15$  at  $\lambda > 4000$  Å. The error bar is larger at 3550 Å and depends on the absolute veiling. This is partially due to poor continuum normalization in this region combined with the effects of low instrumental response. It is usually  $\pm 0.5$ , for values of veiling less than 4.0, and increases to about  $\pm 1.5$  for the largest veiling ( $\sim 8.0$ ). The blend at 3550 Å is not detected on the last night of the May run, preventing any veiling determination in this region.

The complete veiling time series is shown in Figure 6. Also shown are the model-veilings (full line) computed and discussed in section 4.0. The slope of the distribution and the absolute value of the excess at a given wavelength change on short (hours) and long (days) time scales. We will explore the correlation of these changes with other spectral features. For now, we emphasize the daily variations of the veiling parameter, showing the change in absolute values at 4000 Å and 5100 Å (Figure 7 **a,b**), reflecting the variability of the broad B band and the V band (our nearest data point). At the beginning of the May run (JD = 2450942.8846), we find GQ Lupi in a relatively bright state, with an average veiling close to 2.5 in the B band. High cirrus prevented any science on the following night. On JD = 2450944.6867 and the next night, the GQ Lupi veiling is about half of this value. The shapes of the Balmer lines are similar to those reported previously for YY Ori stars, with conspicuous inverse PCygni profiles that are even visible in the red wings of the H & K CaII lines (see Figure 1). The last night of the May run (beginning on JD = 2450947.6066), the veiling recuperates its original strength and the Balmer lines experience the highest emission ever reported for this star - H $\beta$  ranges between 20 and 30 Å). We observe large variations of the continuum in less than 6 hours.

The July time series displays a steady and progressive decrease with local maxima at JD = 2450997.8, 2451000.6 and 2451004.5. The changes near the V band ( $\lambda = 5100$  Å) are similar to those of the B band but less accentuated, especially on the last night of the May run.

Fig. 6.— The veiling spectral distribution is shown for the subset of the GQ Lupi exposures of Figure 1 (dots). Several lines in the Paschen continuum assure a reliable veiling determination in this region. A blend of low excitation potential iron lines is the only probe for veiling in the Balmer continuum region. During the night beginning at JD = 2450947.607, the excess of Balmer continuum flux increases (see Figure 4), preventing any veiling determination at  $\lambda$  3550 with our resolution. The model-veilings developed in section 5 are also indicated.

The continuum excess at  $3550 \text{ \AA}$  relies upon a single measurement and undergoes strong variability. The July run shows a smooth increase in the Balmer jump, with a possible turn over by the end of the observing run, a behavior closely anticorrelated with the veiling. Figure 8 shows how tight this behavior is, especially for the July data set. A similar relation was previously noted by VBJ and GHBC for a set of different CTTS, though with larger scatter.

### 3.2. The Circumstellar Extinction

The SED of a TTS is empirically modeled using an observed photospheric template of the same spectral type and gravity, the veiling distribution of the TTS, and the circumstellar extinction as a free parameter. If the spectrophotometric data is taken during clear nights, both the stellar radius and the circumstellar reddening are consistently and elegantly derived (see GHBC). Our observations were taken under variable atmospheric transmission, which prevented us from determining the stellar radius – a lower limit at best. Thus, we decide to compare only the shape of the empirically modeled SED to the shape of the observed SED. The veiling spectral distribution directly determined from spectroscopy is added to the template photosphere to compose the empirical systemic SED of each exposure (see Eq. [1] in Hartigan et al. 1991). The circumstellar extinction is then inferred after comparing an artificially reddened systemic SED with the corresponding observation. The standard interstellar extinction curve of Cardelli, Clayton & Mathis (1989) is adopted.

For a sufficiently large number of exposures with well computed veiling distributions we thought that the previous exercise would lead us to a single value of circumstellar extinction. On the contrary, we were unable to converge to a single  $A_v$  for one or more of the following reasons. First, the observed flux distribution does not match the modeled SED at  $\lambda < 4000 \text{ \AA}$ . VBJ also notes mismatches between the continuum distribution of their slab models and the observations, within the wavelength range  $3700 - 3900 \text{ \AA}$ . They suspect that errors introduced during the flux calibration procedure affect the final distribution of their adopted flux standard. Our largest source of error is due to a single veiling determination in the Balmer continuum ( $3550 \text{ \AA}$ ), that has the largest error bar in the format ( $\pm 1.5$ ). Thus, extrapolations towards  $\lambda < 4000 \text{ \AA}$  are subject to large uncertainties. Second, and since our data is not flux calibrated, we force normalizations at a given wavelength in order to compare

Fig. 7.— The veiling time series shows smooth variability. We indicate the flux excess at  $4000 \text{ \AA}$  **a)** and  $5000 \text{ \AA}$  **b)**, representing the expected changes in regions near the B and V bands.

the shape of the modeled spectral energy distribution to the observed one. Different values of the circumstellar extinction parameter would prompt changes not only in the shape but also in the flux level of the semi-empirical model. Obviously, our data prevent the latter test, reducing our ability to determine the extinction. Third, the veiling distribution is subject to significant interpolation errors due to sparse sampling. Finally, the small spectral range available to access  $A_v$  ( $\Delta\lambda \sim 1500\text{\AA}$ ) reduces the precision.

Given the above uncertainties, we decide to compute the extinction using the average SED of all of the de-veiled observations. We normalize the 32 de-veiled SED's to the brightest. The resulting curves share similar slopes and deviate less than 10% from the mean at  $\lambda > 4000\text{\AA}$ , increasing up to 20%, at  $3300\text{\AA}$ . The mean curve is assumed to be the GQ Lupi reddened photosphere. The template Gliese 825 (K7 V), is artificially reddened until a sufficient fit to the average reddened photosphere of GQ Lupi is attained. Our data covers a small spectral window, thereby limiting the precision at which the extinction can be inferred. Nevertheless, this exercise leads us to an extinction value of  $A_v = 0.4 \pm 0.2$ . In section 5.1, we develop models of the emitting region and establish an optimum model value within this range.

### 3.3. The $H\beta$ Line Flux Time Series

#### 3.3.1. The Absorption Component

Two components of the  $H\beta$  profiles are clearly distinguished: the emission and the redshifted absorption component, which is indicative of mass infall. The equivalent width of the latter is a rough measure of the column density of obscuring gas crossing the line of sight. Thus, we compute the total depleted area in the extreme red wing of the  $H\beta$  profile, after subtracting the corresponding profile of an inactive photosphere. The results are shown on the left hand side of Figure 9. We are unable to verify any correlation between this absorption and the veiling or the Balmer jump during the May run, perhaps due to the modest number of observations. This perspective is clearly changed in July, however, when the maximum absorption coincides with the maximum veiling in the beginning of the mission. Both parameters decrease steadily up to the end of the mission. Some kinks larger than the uncertainties in the veiling time series are visible at  $\text{JD} = 2451000.469$  and

Fig. 8.— The Balmer jump anticorrelation with the veiling is clearly depicted in this Figure. The May observing run presents a scatter larger than that of the July run. The Balmer jump vanishes for veilings larger than 4.5

2451004.472 but are not reflected in the absorption component. In the left panel of Figure 10, we plot the strength of the continuum excess emission versus the  $H\beta$  absorption component for both the May and July data sets. No trend can be established for the May data set. On the contrary, the July time series shows a clear correlation between the strength of the redshifted absorption and the veiling. Observations with large veiling ( $V_\lambda > 3.0$ ) show strong IPC.

It should be emphasized that these EW's are not corrected for the continuum veiling. As commented in Basri & Batalha (1990) and Hartigan et al. (1991), the inclusion of such corrections would increase the line profile by a factor proportional to the veiling itself ( $1 + V_\lambda$ ), which will further enhance the correlation. The spectrophotometry of Lehmann, Reipurth & Brander (1995), done for EX Lupi, also indicates that the maximum emission – i.e. maximum veiling – coincides with a strong IPC.

The absorption component is completely washed out during the five exposures of May, beginning on  $JD = 2450947.607$ , while the emission components show the strongest emission of the whole time series. Despite the absence of absorption, a column of obscuring material is still feeding the star, and its presence is inferred by the asymmetric shape of the  $H\beta$  emitting profile (see Figure 11). During this particular night, the Balmer jump reaches the highest value of the 1998 -observing season and increases along with the  $H\beta$  strength. Indeed, theoretical predictions (Hartmann 1991) support the correlation between the optical veiling and the strength of the redshifted absorptions. Johns–Krull & Basri (1997) attempt to establish this correlation in DF Tau high resolution time series with no conclusive results.

### 3.3.2. *The Emission Component*

To properly compute the line flux excess, which originates in the circumstellar environment, the underlying photospheric profile which is assumed to be constant, must be subtracted out. Since our data are not of photometric quality, we aim at flux ratios instead. We compute the total emitting line flux normalized to the local continuum. The complete range in variability impressed upon the  $H\beta$  profile during the 1998 observing season is displayed in Figure 11. It is interesting to follow the progression of the absorption minimum and the emission peak as the total emission grows. Both cores move redward as the  $H\beta$  emission strengthens, indicating the progressive depletion of obscuring infalling material out of the line of sight. The strongest absorption coincides with the dimmest emission of the whole series. The blue wing is less subject to variations.

The behavior of the  $H\beta$  emission component as a function of time is shown on the

Fig. 9.— a) The redshifted absorption component of the  $H\beta$  line is measured and presented as a function of time (JD - 2450938). The May time series (left top panel) has a modest data set. On the last observing night, beginning at JD = 2450947.607, the redshifted absorption is not detected, and the emitting component is at a maximum. The absorption component shows regular behavior during the July time series (left bottom panel). The series starts with the absorption near maximum and decreases steadily to a minimum at JD = 2451001.472, strengthening once more thereafter. It should be emphasize that these EW are not corrected for veiling; if they were, the correlation would improve. b) The equivalent width of the  $H\beta$  emission component, not corrected for the veiling continuum emission. The May time series (right top panel) shows the dramatic increase in line emission by the end of the run; the July time series, indicates the steady strengthening of the emission component (right bottom panel).

Fig. 10.— a) The correlation between the veiling and the absorption component is clearly established (left panel). It should be emphasized that if the absorption EW were properly de-veiled, the correlation would strengthen even more. b) On the contrary, the  $H\beta$  emission component is anticorrelated with the excess of continuum emission (right panel, circles). If the emission components are de-veiled, not an obvious change in line fluxes up to veiling of 1.0 is detected. For larger veiling, the line fluxes apparently diminish.

Fig. 11.— The  $H\beta$  lines show, in general, the redshifted absorption components typical of YY Ori stars. At JD = 2450947.607 (May 14<sup>th</sup>), the emission grows to a maximum and no absorption is detected. Nevertheless, the red wings of the profile show clear signatures of depletion, indicating that mass transfer towards the star is still in operation.

right hand side of Figure 9. The line emission detected on the last night of May is unique among our observations. The variations seem to be quite steady on the other nights. The anticorrelation between the emission and the absorption components (compare the left and right middle panel of Figure 9) is striking - even the kinks at  $\text{JD} = 2451000.465$  are seen in reverse.

The veiling is anticorrelated with the observed (not de-veiled) line emission, here indicated by the nominal equivalent width (right panel of Figure 10). However, to properly ascertain the dependency of the line emission on any of the parameters controlling the accretion properties of the gas, proper line de-veiling must be carried out. The de-veiled emission equivalent widths are converted into line fluxes and displayed against the veiling in Figure 10 (stars). We do not find a clear dependence on the continuum excess flux, as found for the absorption component. There is a large scatter at intermediate veilings and the emission fluxes of May 14th are off scale. We note an apparent dimming of line emission at veilings larger than 3.20, perhaps indicative of a real intrinsic weakening of line emission as veiling grows. However, the trend is not conclusive because of the low resolution of the data. The emission component is next to a variable and –for high veiling cases – stronger component that is in absorption. High resolution  $\text{H}\beta$  time series should be taken in order to confirm if the line emission properties – which are primarily dependent on the circumstellar environment – vary along with the changes in the shock region.

Changes in the veiling are governed by variable  $\dot{M}$  or by changes in the field configuration which will affect the density and/or temperature of gas where the excess continuum emission originates. Figure 10 indicates that line emission is primarily ignoring whatever changes might be operational at the bottom of the accreting funnel. As veiling grows, so does the absorption along the line of sight that will translate into larger inverse PCygni absorption. The line flux emission, on the contrary, depends primarily on the hydrodynamic properties of the accreting gas, such as the local gas density and temperature and the velocity field.

### 3.4. The Brightening of GQ Lupi on $\text{JD}=2450947.607$

The smooth variability of the spectral features discussed herein is met with one exception. On  $\text{JD} = 2450947.607$ , most of the measured parameters reveal their extremes: large veiling at  $4000 \text{ \AA}$ , the largest Balmer jump, the largest Balmer and CaII emission lines, along with the simultaneous appearance of the Fe II emission lines. The inverse PCygni profiles are not detected, and the largest variability in the Balmer lines and Balmer continuum are also measured. If veiling corrections are included to recuperate the real profile, the  $\text{H}\beta$  emission peak nearly doubles. This tendency is not verified on other nights.



The strengthening of the Balmer continuum emission can be inferred by the complete absence of the  $\lambda$  3550 blend of iron absorption lines. Thus, Balmer continuum veiling is not measured this night. The sudden flux increase of the Balmer continuum, as shown in Figure 4, is not followed by a similar brightening of the Paschen continuum. The slope of the latter suffers negligible changes (see the open circles Figure 5 **a,b**) while the jump strengthens. In fact, the flux excesses displayed in Figure 6 reflect this behavior: the average veiling distribution at  $\lambda > 4000 \text{ \AA}$  does not change with the sudden increase of the Balmer continuum, strongly supporting distinct formation regions for both spectral features on this particular night. However, a common region of formation can be argued if the Balmer jump increase is the result of a slightly higher gas temperature and significantly higher filling factor (see Section 4.5).

## 4. Discussion

### 4.1. The Balmer Jump *vs* Veiling Anticorrelation

The continuum excess flux anticorrelates with the Balmer jump (Figure 8). This trend was first reported by VBJ, using a large sample of TTS and was interpreted within the slab scenario as a competition between the  $\text{H}^-$  and the  $\text{H}_{b-f}$  opacities for a given gas density and temperature. For low hydrogen densities, negligible amounts of  $\text{H}^-$  form, and the jump depends only on the slab temperature. As the density increases – a direct result of increasing mass infall or decreasing slab projected area – the growing concentration of  $\text{H}^-$  governs the emission at the jump and eventually washes it out.

The anticorrelation is also verified by GHBC, and they comment on the large optical thickness of the emitting source to diminish the jump. Nevertheless, they suggest that distinct regions might be producing the Balmer and the Paschen continua. Since stars of high accretion rate tend to show negligible Balmer jumps, they conclude that the Paschen continuum must increase faster than the Balmer continuum.

Shock models developed by CG suggest that the Balmer excess is produced in the pre-shock region and is optically thin. The flux excess along the Paschen continuum is optically thick, arising in regions of the stellar atmosphere where the bulk of accreting energy is reprocessed. The emission lines are formed preferentially along the magnetic funnel if a certain configuration for the magnetic field is assumed (Hartmann et al. 1994; Muzerolle, Calvet & Hartmann 1998). Allowing different regions to contribute to the final spectral distribution is an improvement over earlier slab models – especially if the asymmetric shapes and signatures of inverse PCygni profiles are taken into consideration. In this scenario,

the veiling anticorrelation with the Balmer jump is understood if the Paschen continuum, which is governed by the mass infall, grows more rapidly than the Balmer continuum as the accretion increases.

#### 4.2. What Governs the Reported Variability?

The accretion flow onto the central star affects several observables in the optical range: the excess continuum of the Balmer and Paschen regions, the total emission line fluxes, the shape of the line profile and the strength of the absorption feature of the (inverse) PCygni profiles. One of the primary motives in time series observations of pre–Main Sequence stars is to determine the extent to which the emitting quantities present periodic behavior comparable to the photometric periods of the central star, when available. Thus, we turn our attention to previous photometry of GQ Lupi. This star does not yet have a photometric period set in the literature. Covino et al. (1992) publish light curves taken over 13 nights, but the time sampling is not adequate for a firm period determination. We note, however, that the local V band flux minimum repeats its approximate value about 12 days later. P.C.Pereira (private communication) also notes similar behavior after analyzing his unpublished photometry. One can understand the difficulties involved in establishing periodic behavior of GQ Lupi by observing the veiling time series depicted in Figure 7 **a,b**: an increase of about 1 mag in the B band during the 8 nights of July, with two local maxima (in flux). We submit the veiling time series to a periodogram analysis with no conclusive results. If the stellar magnetosphere is bipolar, the accreting gas will fall at high latitudes. Since GQ Lupi shows inverse PCygni profiles in general, it is feasible to assume that the system is observed with the line of sight nearly aligned with the infalling column of gas, and that a large fraction of the reprocessed energy of the accretion shock remains in view as the star rotates. The major determinant in the changes are the field line configurations and/or the variable mass accretion resulting from the disk inhomogeneities. We develop models of the emitting region to identify which of these possibilities governs the continuum and the line changes.

#### 4.3. Slab Models and the Continuum Emission

We approach the continuum emitting region with the simplest scenario to treat a smooth flux continuum change: a slab of uniform density and temperature. The observed variability is governed by changes in the temperature, density or geometrical scale of the slabs. Previous slab models have explained some of the observations of a large set of CTTS (see VBJ).

GHBC computes slabs with particle densities of  $N_H = 10^{14} \text{ cm}^{-3}$  and three different regimes of opacity ( $\tau_{3640} \sim 0.1, 1.0, 10.0$ , respectively). They show that optically thick slabs of high temperatures ( $\sim 10000 \text{ K}$ ) are compatible with the observed Balmer jump and the Paschen continuum slope, but inconsistent with the observable Balmer continuum slope. The latter indicates gas emitting regions of smaller temperatures. A natural improvement over slab models is the accretion shock model of CG in which the Balmer and the Paschen slopes as well as the Balmer jump are simultaneously matched. Contrary to the basic premise of slab models, their accretion shock models establish different regions for each of the continua. While the Paschen continuum emission is kinetic energy released and reprocessed in the after shock region, the Balmer continuum originates in the optically thin gas of the pre-shock region in the upper photosphere. Our choice for using a simple approach is to determine which of the key gas parameters governs the flux changes of the time series and not to develop precise models.

The general code CLOUDY is adopted to compute the radiation field of such a slab. The choice of CLOUDY is based on its simplicity and flexibility in the choice of the external velocity field, unimportant for calculations of the continuum flux but important in the calculations of line formation. NLTE populations are computed and input into an independent code to compute the line profiles (Lopes & Batalha – in preparation). The standard continuum opacity sources are included, including that of  $\text{H}^-$ . For each hydrogen density, the statistical equilibrium equations of a 15–level atom are solved, and all collisional and radiative processes are included. The composed systemic SED is  $F_\lambda = (1 - \delta)F_{ph} + \delta (F_{ph}e^{-\tau} + F_{slab})$ , where  $\delta$  is the projected slab area (filling factor in % of the stellar full disk area),  $F_{ph}$  and  $F_{slab}$  are the photospheric and the slab flux distributions respectively, and  $\tau$  is the slab optical depth.

We adopted the newly released version in C, that provides reliable results for the range of densities and temperatures explored in this paper. We extend the gas densities up to blackbody limits for a characteristic temperature and allow the geometric extent of the slab to reach 1500 km (steps of 500 km), about twice the average thickness of all models of VBJ. A grid of slabs models with densities larger than  $N_H > 10^{13} \text{ cm}^{-3}$ , temperatures within the range  $5000 \text{ K} < T_e < 12000 \text{ K}$ , in steps of 100K, are computed, and the resulting distribution,  $F_\lambda$ , compared directly to the de-reddened data. We adopt filling factors starting at 0.05% and extending up to 20 % of the stellar surface. For densities less than  $10^{14} \text{ cm}^{-3}$ , the Balmer jump of the slab, diluted by the photospheric radiation, is larger than any of those observed. The impact of the  $\text{H}^-$  ion in the total opacity budget is negligible and the opacity is controlled by hydrogen bound–free transitions. As the gas density increases, the growing collisional rates eventually govern the statistic equilibrium, causing the spectral energy distribution to approach a Planck function. The Balmer continuum meets the blackbody distribution first,

followed by the Paschen continuum.

#### 4.4. Modeled Slab Parameters

Allowing all possible free parameters to float (temperature, slab dimensions and gas density), we search for a combination of gas parameters providing optimal fits to the observed SED’s (the Balmer jump and the slopes of the Balmer and the Paschen continua). The circumstellar extinction is constrained to  $A_v = 0.4$  mag (see section 3.2). Each SED is defined by 14 continuum windows, including one at  $3860 \text{ \AA}$  that constrains the apparent absorption blend of the photospheric CN, CaII H & K and hydrogen outer wings. Although we are able to obtain sufficiently good fits to the observed SED’s, the models do not reproduce the observed veiling distribution for the exposures of large Balmer jumps. More specifically, the models underestimate the veiling at  $4000 \text{ \AA}$ , even if extinctions larger than 0.4 mag are considered. By increasing the circumstellar extinction, hotter slabs have to be considered to compensate for the depleted blue continuum, thereby pumping the blue veiling. However, models of slightly larger chi-squared, discarded during the model search procedure, are found to provide simultaneous fits to the SED and to the veiling distribution. Final solutions are therefore chosen to be those which fit both the SED and veiling distribution. The final slab parameters are listed in Table 2 along with the relative standard deviations about the final fits. The time series of the model parameters are displayed in Figure 12, and the actual fits to the sub-set of observations displayed in Figure 1 are shown in Figure 13. Final model veilings are plotted in Figure 6. As mentioned in Section 2.2, light losses were registered on  $\text{JD} = 2450944.687$  and  $\text{JD} = 2450945.826$ , thereby affecting the observed SED. Those model parameters are displayed with open circles in Figure ?? and Figure ??.

We emphasize the importance of using the veiling distribution to constrain models of continuum emitting regions as degenerate solutions appear to be problematic (see VBJ). Knowledge of the veiling in a small wavelength window (e.g. at  $\lambda 4226 \text{ \AA}$ – a commonly used region for veiling determination) may result in degenerate solutions as well.

Fig. 12.— The slab model time series indicate a smooth variation of parameters on a night-to-night basis. Open circles indicate nights in which light losses were registered

#### 4.5. Correlations Among Modeled Parameters

We analyze the correlations among the model parameters to infer the dynamics of the region where the excess continuum originates. The slab temperature governs the slope of the Balmer continuum while the slab density (and to a lesser degree the slab projected area ( $\delta$ )) constrains the size of the Balmer jump. Temperature and density are anticorrelated (Figure 14a), and the total emitting area increases with the gas density. That is, models yielding a low density slab of higher temperature have small emitting areas. Increasing the density of a slab of a given temperature enhances the excess emission, and the distribution approaches the blackbody. Since the observed veiling distribution and the Balmer jump both constrain the models, one has to decrease the slab temperature to keep the model flux excess within the observed values if the gas density grows.

The filling factor is the total projected area where the kinetic energy of the accretion is released. It grows for larger densities and lower temperatures. We interpret this growth as a direct consequence of mass accretion towards the central star, where the energy released in the after shock region is imparted over larger areas.

The trends between the veiling and the model parameters are shown in Figure 14 **b**. Large optical continuum excesses are the result of large gas densities spreading over larger areas. Low veiling observations yield slab models of small projected emitting areas and larger temperatures. The anticorrelation between the veiling and the Balmer jump (Figure 8) is driven by density changes: the  $\tau_{Balmer}$  is already opaque, and the Balmer continuum distribution follows that of a blackbody of a given temperature (slope of Balmer continuum determines slab temperature). As  $\tau_{Paschen}$  increases, the Paschen spectral distribution merges with the blackbody distribution, which is an extension of the Balmer continuum. Veiling increases, and the jump gradually disappears. The models indicate that the largest veiling states of GQ Lupi have filling factors larger than the series average and slab temperatures lower than the series average.

Based on the nearly constant presence of IPC in the Balmer lines, it is possible to apply the magnetic field accretion scenario (Calvet and Hartmann 1992) to mediate the gas

Fig. 13.— Slab models are computed for the sub-sample of the GQ Lupi exposures presented in Figure 1 (dotted line). The best model (filled line) provides the minimum residual to the observation and fits the observed veiling. The geometrical thickness of the slab is found to be 1000 km, and the best model is chosen out of a grid of varying  $N_H$  ( $1.0 \cdot 10^{13} - 1.0 \cdot 10^{17}$ ),  $T_e$  (5000 K – 16000 K) and filling factors (0.0005 – 0.20). The model parameters are listed in each panel. The corresponding model-veiling are displayed in Figure 6.

accretion and to establish where the continuum emission originates. The model parameters should indicate where the slab rests. Assuming that the gas is free-falling from a certain position  $R_i$  in the circumstellar disk, the resulting disk accretion rate is (CG. see their eq. [6]):

$$\left(\frac{\dot{M}}{10^{-8} M_{\odot} \text{ yr}^{-1}}\right) = \left(\frac{N_H}{5.210^{12}}\right) \left(\frac{M}{0.5 M_{\odot}}\right)^{1/2} \left(\frac{R}{2 R_{\odot}}\right)^{3/2} \left(\frac{\delta}{0.01}\right) \left(1 - \frac{R_{\star}}{R_i}\right)^{1/2}$$

The computed number density for the highest veiling exposure at JD = 2450997.7525 is  $N_H = 2.2 \cdot 10^{15} \text{ cm}^{-3}$ . The resulting accretion rate is larger than  $10^{-5} M_{\odot} \text{ yr}^{-1}$  which is too high for a classical TTS of modest veiling such as GQ Lupi. This density is that of a stellar photosphere with a mass column of  $0.2 \text{ gr cm}^{-2}$ , characterized by temperatures in the range 6000 - 9000 K. Thus, the slab is not located in the accreting gas funnel between the circumstellar disk and the shock region. Rather, the mass column is located in the photosphere adjoined to the base of the magnetic funnel, where the accretion energy is released.

The accretion luminosity ( $L_{acc}$ ) is proportional to  $\delta F$ , where F is obtained by integrating  $F_{ext}$  (see Figure 6) over the entire spectrum. Figure 14 indicates that the veiling ( $F_{ext}/F_{phot}$ ) grows in cadence with the filling factor ( $\delta$ ), suggesting that the accretion luminosity increases with the veiling. This leads us to conclude that the progressive decrease of the accretion rate ( $\dot{M} \propto L_{acc}$ ) during the July time series governs the changes in the veiling and IPC absorption. The weakening  $\dot{M}$ , however, does not prevent the reprocessed atmospheric gas from heating, perhaps indicating that more of the region near the footpoint of the accretion column is being progressively exposed.

We look for other trends between the temporal behavior of the slab parameters and spectral features that are clearly produced in a physically detached region. The redshifted absorption component, for instance, probes the infalling gas outside the atmosphere while the optical veiling is the reprocessed energy of the gas accretion onto the atmosphere. The redward absorption, which is dependent on the number of absorbers along the line of sight, is large for large values of  $\delta$  (or  $\dot{M}$ ) and weakens for decreasing  $\delta$  (see Figure 9 and Figure 12 in the July run). Due to the YY Ori aspect of the GQ Lupi line profiles, one can speculate that GQ Lupi is observed with the line of sight nearly aligned with the funnel axis. Thus, for larger continuum emitting areas ( $\delta$ ), more of the infalling gas will absorb and deplete the underlying continuum. This trend, however, is not seen on the last night of the May run. The total emitting area is among the largest we model and we detect no redshifted absorption. It is possible that the strong hydrogen emission on this particular night overcomes the absorption and fills it in. Theoretical efforts of Hartmann et al. (1994) predict that inverse

PCygni profiles will occur if an emitting region hotter than the photosphere lies at the base of the accreting column of gas. Surely, the absorption we measure depends on the shape and emitting characteristics of the slab.

Given the fact that the Paschen continuum near the jump is not completely thick, emission line components will necessarily be formed in the slab. Such emission lines were formerly modeled in VBJ. However, and especially for the low Balmer lines ( $H\beta$  in our case), the core of the emission will be preferentially produced external to the slab. For  $H\beta$ , we note that the emission component varies less than the redshifted absorption or the veiling (see Figure 10), indicating that the bulk of the emission is governed by the morphology of the magnetic field lines and the state of the controlled gas.

## 5. Summary

We have presented time series spectrophotometric observations of GQ Lupi, a well known member of the YY Ori sub-class of T Tauri stars characterized by inverse PCygni profiles in the Balmer lines – a clear signature of mass infall. The sample comprises a total of 32 exposures distributed over 13 nights in May and July 1998. In spite of the low resolution of the data, we recover the excess flux distribution (i.e. veiling) throughout the region of the Paschen continuum and, in most of the cases, in the Balmer continuum at  $3550 \text{ \AA}$ .

We summarize the major observational results as follows

1) The strength of the Balmer jump, defined as the flux ratio between the extrapolated Paschen and Balmer continua towards the jump, presents, in general, smooth variability (see Figure 3).

2) The veiling time series also shows smooth and steady variability on a night-to-night basis (see Figure 6 **a**, **b**), and the largest flux excesses are measured in the Balmer continuum. We confirm the previous findings of VBJ and GHBC, based on a large sample of CTTS, that the veiling anticorrelates with the Balmer jump (see Figure 8).

3) The constant presence of inverse PCygni profiles is the major characteristic of a YY Ori star. This fingerprint disappears from all of the Balmer and the CaII H & K lines on the last night of the May run (1 out of 13 nights). Nevertheless, signatures of mass infall

Fig. 14.— **a** The temperature and the density distribute themselves along a perfect locus. The filling factor grows towards low temperatures. **b** The correlation between the veiling and the model parameters.

towards the central star are impressed in the emission lines (see Figure 11).

4) The observed and not de-veiled equivalent widths of the  $H\beta$  redward absorption are correlated with the excess continuum emission (see Figure 10, left). On the contrary, the de-veiled  $H\beta$  emission flux components do not change significantly for veiling less than 1.1 ( $V\lambda = 4000 \text{ \AA}$ ), although large scatter is verified at intermediate veiling. The emission weakens at larger veiling (see Figure 10, right, and crosses).

5) The apparently modest variability of the GQ Lupi continuum is not a rule. In a series of observations taken on JD 2450947.607, the Balmer continuum shows flux excesses which grow to larger than 10 times the photospheric value, and the Balmer lines brighten well above the average value of the series. The Balmer jump is at a maximum this particular night.

We model the observed continuum emission assuming it incorporates contributions from the stellar photosphere  $[(1 - \delta) F_{ph}]$  and from a slab of uniform temperature, particle density and height  $[\delta(F_{slab} + F_{ph}e^{-\tau})]$ , where  $\delta$  is the projected area in % of the stellar photosphere and  $\tau$  is the slab opacity. The circumstellar extinction for GQ Lupi is found to be  $A_v = 0.4$ . The computed models reproduce the Balmer and the Paschen continuum slopes, the Balmer jump (see Figure 12) and the veiling distribution (see Figure 6). We summarize the major results as follows:

1) The slab temperature governs the slope of the Balmer continuum, while the gas density and filling factors determine the size of the jump and the slope of the Paschen continuum. Thus, changes in the mass column density of the slab – not in the gas temperature – govern the veiling and the size of the Balmer jump.

2) The slab temperatures are strongly anticorrelated with the slab gas densities, defining a perfect locus. The slab projected area increases with the density. We position the slab in the stellar atmosphere near the shock region, where the free falling gas reaches the stellar surface.

3) Models of large densities, large emitting areas and low temperatures fit all the data characterized by  $H\beta$  with strong inverse PCygni profiles. In general, models of lower density and larger temperature fit data of mildly redshifted absorption and large Balmer jump.

The slabs are optically thin redward of the Balmer jump. Consequently, some component of the higher Balmer lines are likely to be produced in the slab. For the lower Balmer lines, most of the emission originates in either a magnetically mediated accretion flow or in an expanding gas. The  $H\beta$  lines show inverse PCygni profiles indicating their circumstellar origin. When the observed  $H\beta$  redward absorption is largest, the modeled slab density is at



its highest for the series. The density steadily decreases as the absorption component weakens. The optical veiling is tightly correlated with the  $H\beta$  redward absorption strength. The emission component is much more steady throughout the series, showing less dependence on the physical conditions of the post-shock region.

The atmosphere near to the shock region responds to the diminishing accretion rate ( $\dot{M}$ ), showing less veiling and being confined to smaller areas ( $\delta$ ). On the contrary, the gas temperature grows as does the observed Balmer jump. Additional spectrophotometric and high resolution data of GQ Lupi are currently being analyzed to investigate how these trends evolve with time.

We thank G. Ferland for making available the latest version of CLOUDY before releasing it. We thank M. Fernandez for the careful reading of an earlier version of this paper. N.B. acknowledges the support of the Fundação de Amparo à Pesquisa do Estado do Rio de Janeiro (FAPERJ).

## REFERENCES

- Adad, A., Appenzeller, I., Bertout, C., Isobe, S., Shimizu, M., Stahl, O., Walker, M. F., & Wolf, B. 1984, *A&A*, 130, 67
- Appenzeller, I., Chavarria, C., Krautter, J., Mundt, R. & Wolf B. 1980, *A&A*, 90, 184
- Appenzeller, I., Mundt, R., & Wolf, B. 1977, *A&A*, 63, 289
- Appenzeller, I., & Dearborn, D. S. R. 1984, *ApJ*, 278, 689
- Appenzeller, I., Jankovics, I., & Krautter, J. 1983, *A&AS*, 53, 291
- Appenzeller, I., & Wolf, B. 1977, *A&A*, 54, 713
- Basri, G., & Bertout, C. 1989, *ApJ*, 341, 340
- Bertout, C., Basri, G., & Bouvier, J. 1988, *ApJ*, 330, 350
- Bertout, C., Carrasco, L., Mundt, R., & Wolf, B. 1982, *A&AS*, 47, 419
- Calvet, N., & Gullbring, E. 1998, *ApJ*, 509, 802 (CG)
- Calvet, N., & Hartmann, L. 1992, *ApJ*, 386, 239
- Camenzind, M. 1990, *Reviews in Modern Astronomy* (Springer-Verlag: Berlin), 3, p. 234

- Cardelli, J. A., Clayton, G. C., & Mathis, J. S. 1989, *ApJ*, 345, 245
- Covino, E., Terranegra, L., Franchini, M., Chavarria, K., & Stalio, R. 1992, *A&AS*, 94, 273
- Edwards, S. 1979, *PASP*, 91, 329
- Filippenko, A. V. 1982, *PASP*, 94, 715
- Giampapa, M. S., Basri, G., Johns, C. M., & Imhoff, C. L. 1993, *ApJS*, 89, 321
- Grasdalen, G. 1977, *Proceedings of IAU Colloquium 42*, eds. R. Kippenhahn, J. Rahe, and W. Strohmeier, p.25
- Gullbring, R., Hartmann, L., Briceno, C., & Calvet, N. 1998, *ApJ*, 492, 323 (GHBC)
- Gullbring, E., Petrov, P. P., Ilyin, I., Tuominen, I., Hackman, T., & Loden, K. 1996, *A&A*, 314, 835
- Jacoby, G. H., Hunter, D. A., & Christian, C. A. 1984, *ApJS*, 56, 257
- Johns, C. M., & Basri, G. 1995a, *ApJ*, 449, 341
- Johns, C. M., & Basri, G. 1995b, *AJ*, 109, 2800
- Johns–Krull, C. M., & Basri, G. 1997, *ApJ*, 474, 433
- Hamuy, M., Walker, A. R., Suntzeff, N. B., Gigoux, P., Heathcote, S. R., & Phillips, M. M. 1992, *PASP*, 104, 533
- Hartigan, P., Kenyon, S. J., Hartmann, L., Strom, S. E., Edwards, S., Welty, A. D., & Stauffer, J. 1991, *ApJ*, 382, 617
- Hartmann, L., Calvet, N., Avrett, E. H., & Loeser, R. 1990, *ApJ*, 349, 168
- Hartmann, L., & Calvet, N. 1992, *ApJ*, 386, 239
- Hartmann, L., Hewett, R., & Calvet, N. 1994, *ApJ*, 426, 669
- Herbig, G. H., & Bell, K. R. 1988, *Lick Obs. Bull.* 1111
- Königl, A. 1991, *ApJ*, 370, L39
- Krauter, J., & Bastian, U. 1980, *A&A*, 88, L6
- Lago, M. T. V. T., & Gameiro, J. F. 1998, *MNRAS*, 294, 272

- Lehmann, T., Reipurth, B., & Brandner, W. 1995, *A&A*, L9
- Lopes, D. F., & Batalha, C. 1999, in preparation
- Mundt, R. 1983, *ApJ*, 1984, 280, 749
- Mundt, R. 1984, *ApJ*, 280, 749
- Muzerolle, J., Calvet, N., & Hartmann, L. 1998, *ApJ*, 492, 743
- Petrov, P. P., Gullbring, E., Ilyin, I., Gahm, G. F., Tuominen, I., Hackman, T., & Loden, K., 1996, *A&A*, 314, 821
- Shu, F., Najita, J., Ostriker, E., Wilkin, F., Ruden, S., & Lizano, S. 1994, *ApJ*, 429, 781
- Stout – Batalha, N.M., Batalha, C., & Basri, G. 2000, in press.
- Uchida, Y., & Shibata, K. 1984, *PASJ*, 36, 105
- Valenti, J. A., Basri, G., & Johns, C. M. 1993, *AJ*, 106, 2024 (VBJ)
- Walker, M. F. 1972, *ApJ*, 175, 89
- Wolf, B., Appenzeller, I., & Bertout, C. 1977, *A&A*, 58, 163

Table 1. 1998 Observing Log of GQ Lupi

JD (mid.exp.)	date	weather transp. %
2450942.8846	5/09	20
2450942.9252	5/09	
2450944.6867	5/11 <sup>@</sup>	>40
2450945.8255	5/12 <sup>@</sup>	
2450947.6066	5/14	35
2450947.6748	5/14	
2450947.8357	5/14	
2450947.9003	5/14	
2450947.9108	5/14	
2450997.5107	7/02	20
2450997.6179	7/02	
2450997.7525	7/02	
2450998.4735	7/03	17
2450998.6319	7/03	
2450998.7088	7/03	
2450998.7810	7/03	
2450999.4673	7/04	29
2450999.6339	7/04	
2450999.7539	7/04	
2451000.4648	7/05	15
2451000.6232	7/05	
2451001.4743	7/06	>40
2451001.7369	7/06	
2451001.7786	7/06	
2451002.6388	7/07	40
2451002.6922	7/07	
2451002.7618	7/07	
2451003.4727	7/08	35
2451003.6624	7/08	
2451003.7468	7/08	
2451004.4716	7/09	27
2451004.7120	7/09	

<sup>@</sup>Light losses were registered (see text) and the SED is not reliable

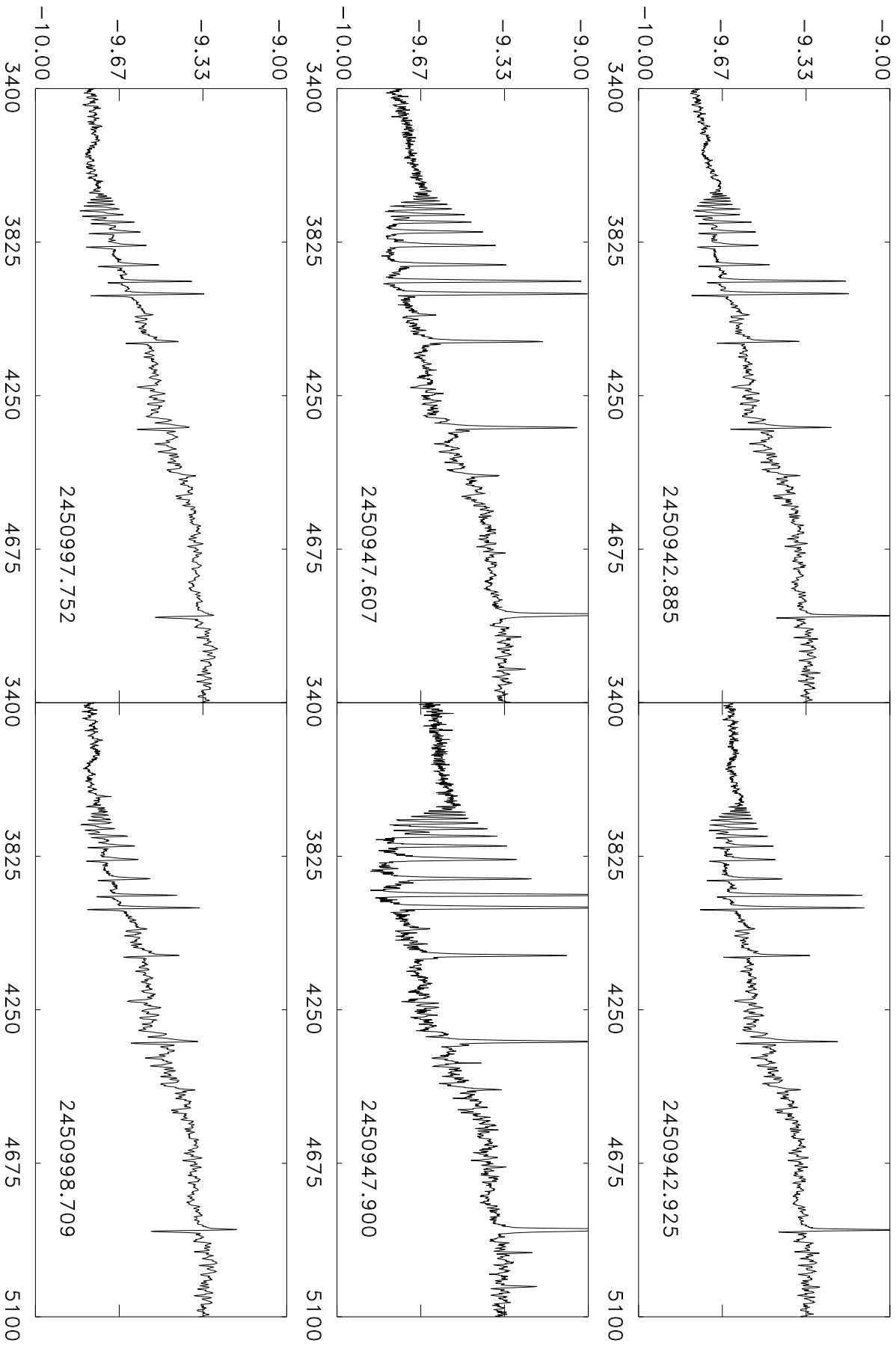
Table 2. Slab Model Parameters

JD (mid.exp.)	$N_H$ *	T (K)	$\delta$ (%)	$\chi^2$ **
2450942.8846	3.50	7200	5.2	0.92
2450942.9252	1.10	8000	5.6	1.86
2450944.6867 <sup>ⓐ</sup>	9.90	6100	8.6	0.87
2450945.8255 <sup>ⓐ</sup>	1.60	7800	2.8	0.88
2450947.6066	4.10	6700	9.4	1.07
2450947.6748	5.50	6700	9.9	2.86
2450947.8357	3.20	6900	9.0	1.37
2450947.9003	1.20	7800	5.4	2.48
2450947.9108	0.68	8200	3.6	1.36
2450997.5107	1.40	7900	5.0	1.22
2450997.6179	2.20	7600	5.6	0.62
2450997.7525	2.20	7600	5.6	0.62
2450998.4735	1.90	7700	5.0	1.59
2450998.6319	2.10	7600	5.0	2.00
2450998.7088	1.10	8100	4.2	0.79
2450998.7810	1.00	8200	4.4	0.11
2450999.4673	1.40	7900	3.0	0.32
2450999.6339	1.80	7700	2.4	0.68
2450999.7539	1.60	7800	2.4	0.88
2451000.4648	1.20	8000	3.8	0.66
2451000.6232	0.54	8600	3.8	0.47
2451001.4743	0.38	9000	2.2	1.85
2451001.7369	0.35	9100	1.4	1.96
2451001.7786	0.34	9100	1.6	3.04
2451002.6388	0.51	8600	1.8	0.72
2451002.6922	0.47	8700	1.6	1.57
2451002.7618	0.41	8800	1.6	1.88
2451003.4727	0.37	8900	1.0	3.50
2451003.6624	0.40	8700	1.2	2.03
2451003.7468	0.42	8800	1.6	2.39
2451004.4716	2.00	7500	3.0	0.55
2451004.7120	1.20	7900	2.4	0.39

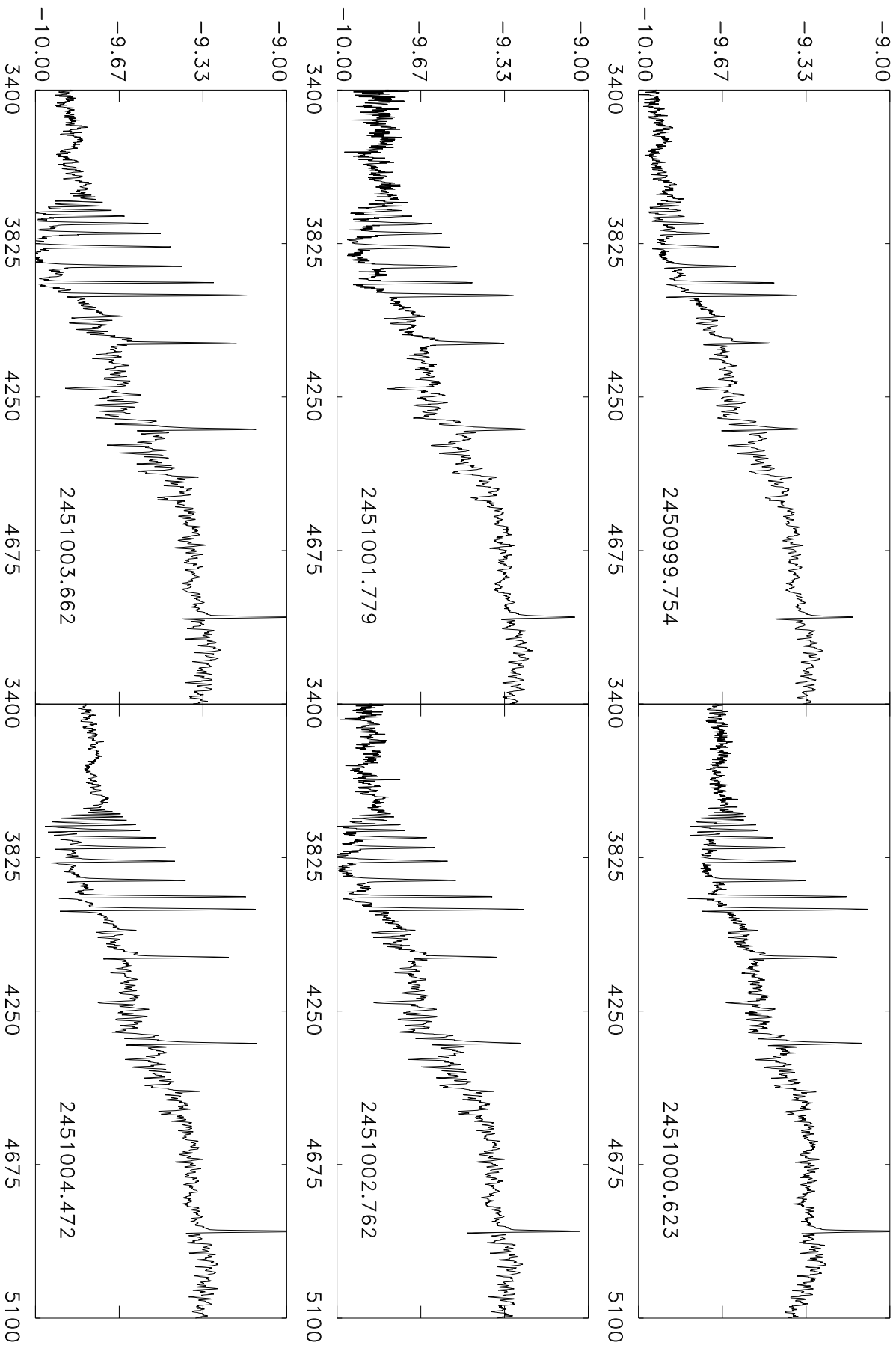
\* $N_H$  in unities of  $10^{15} \text{ cm}^{-3}$ .

\*\*  $\chi^2$  is defined as  $10^4 (F_{mod} - F_{obs})^2 / F_{obs}^2$ .  $F$  is Log(flux). Acceptable solutions have  $\chi^2$  less than 50.

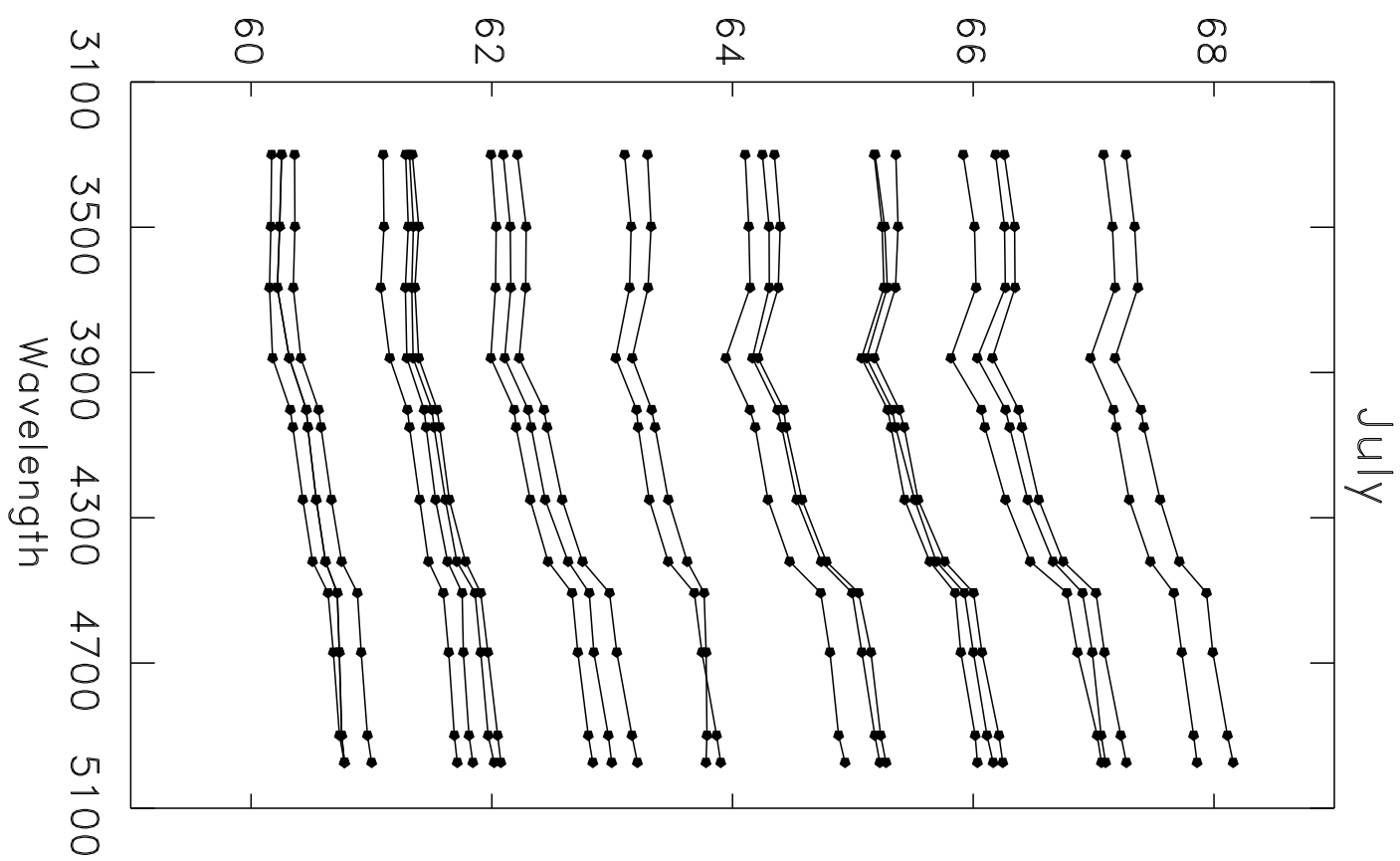
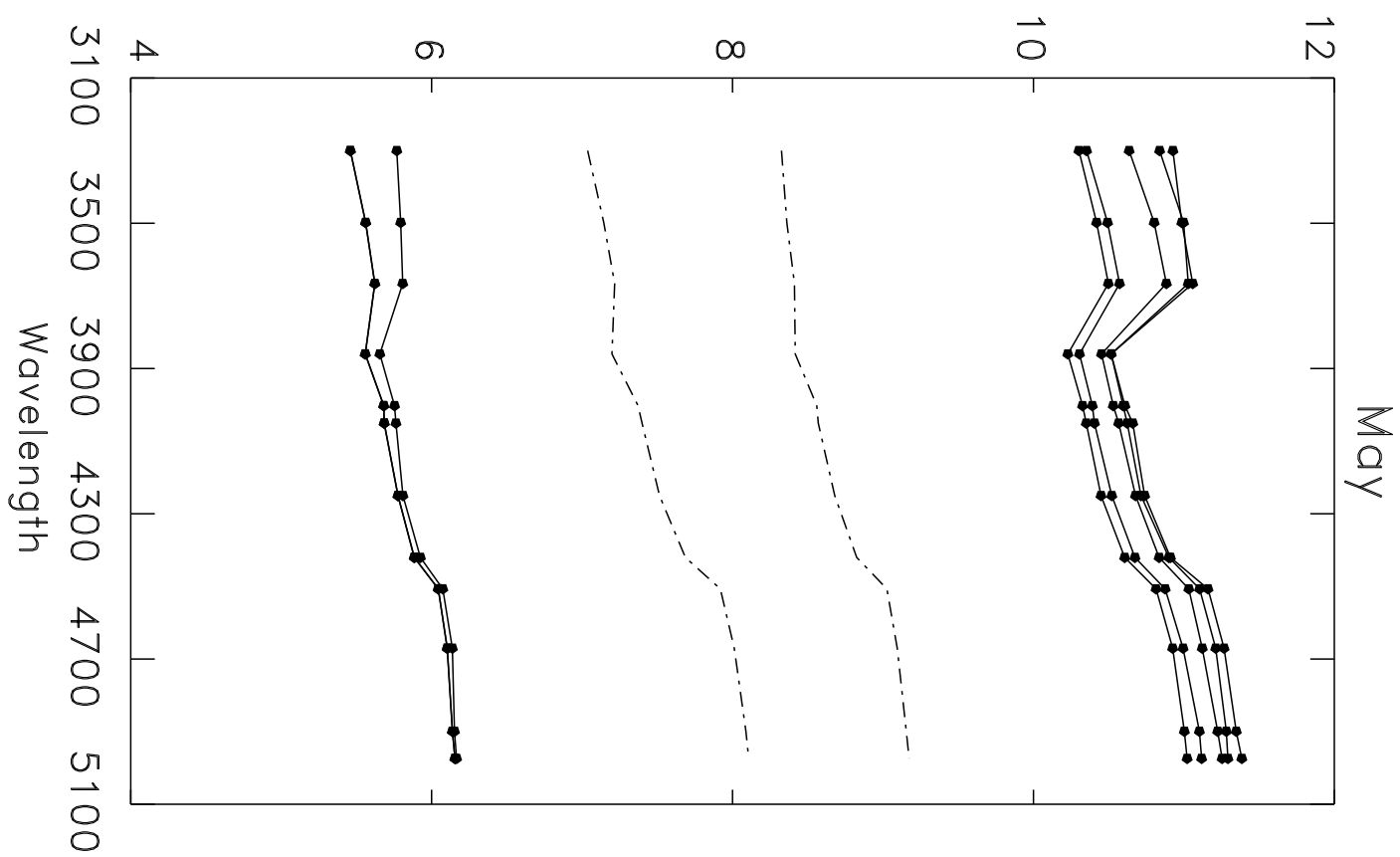
$\text{Log } \lambda F_\lambda \text{ (erg/cm}^2\text{/seg)}$



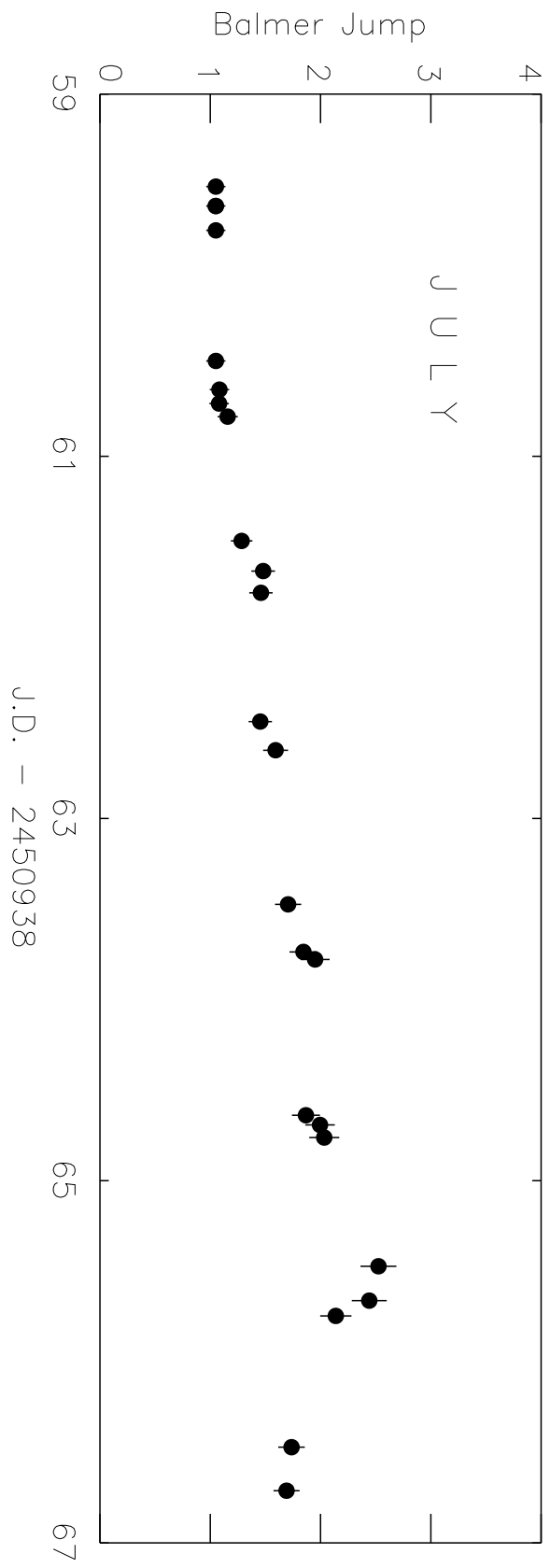
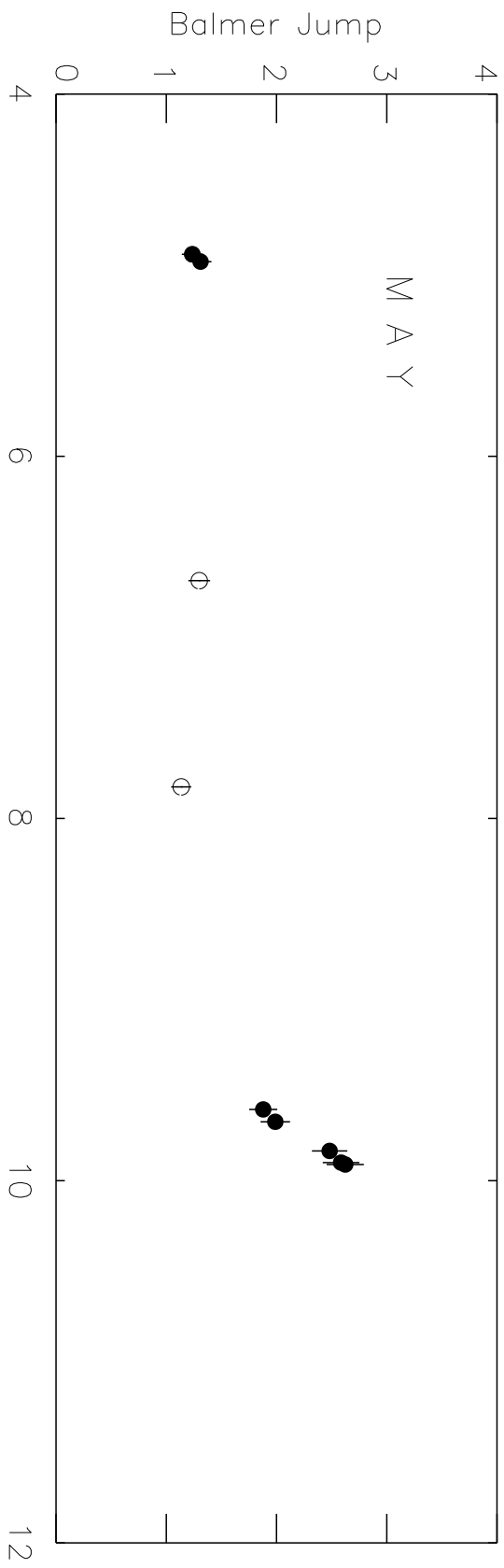
Log  $\lambda F_\lambda$  (erg/cm<sup>2</sup>/seg)



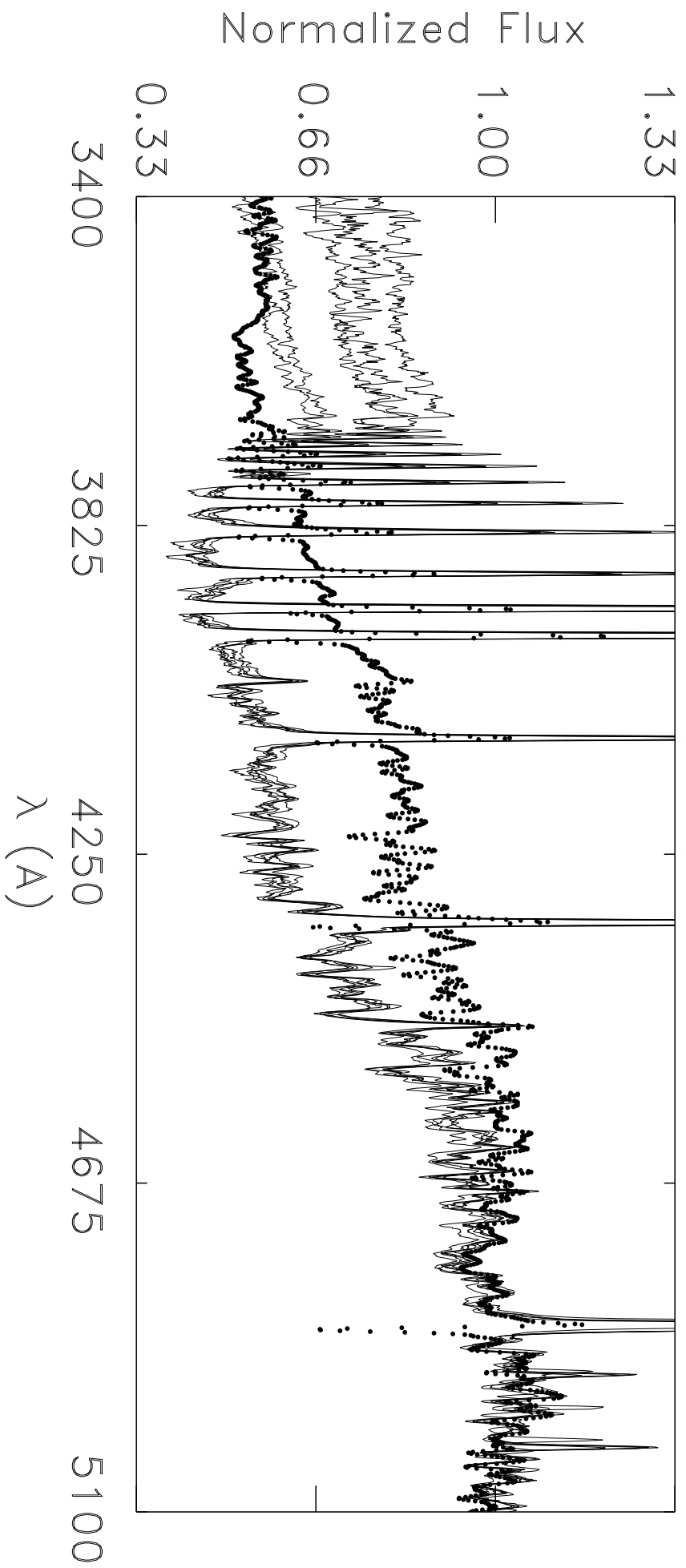
JD - 2450938

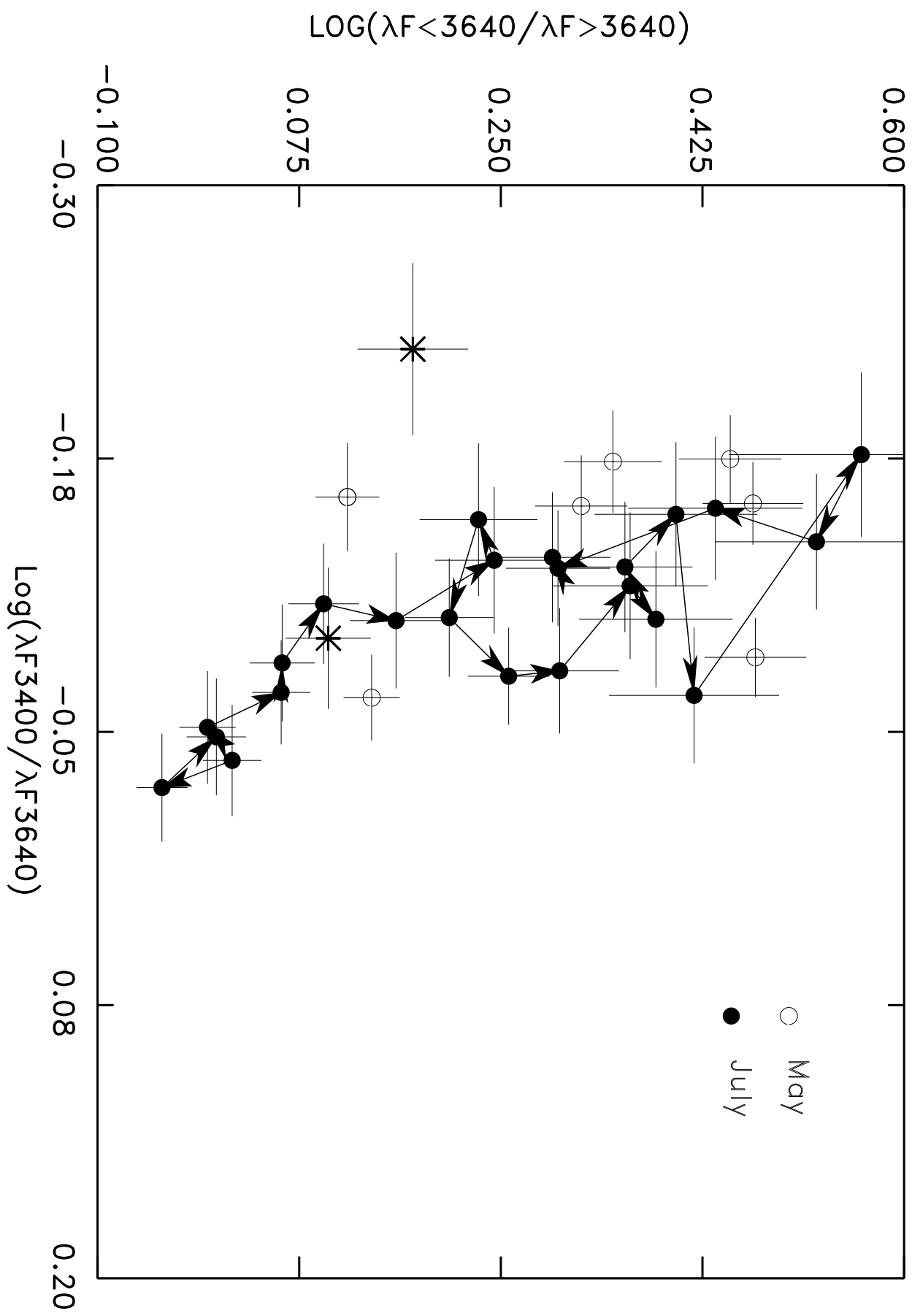


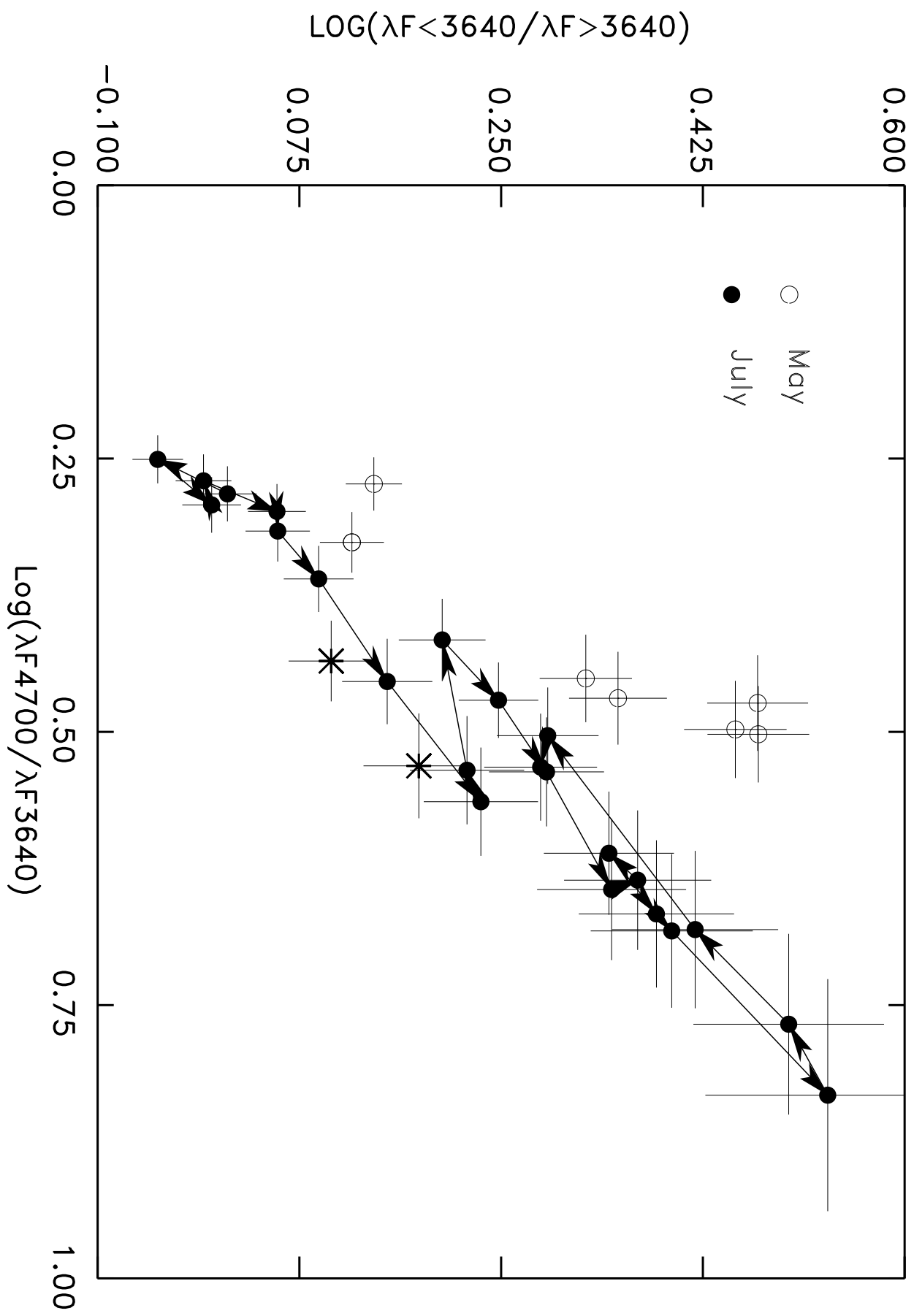


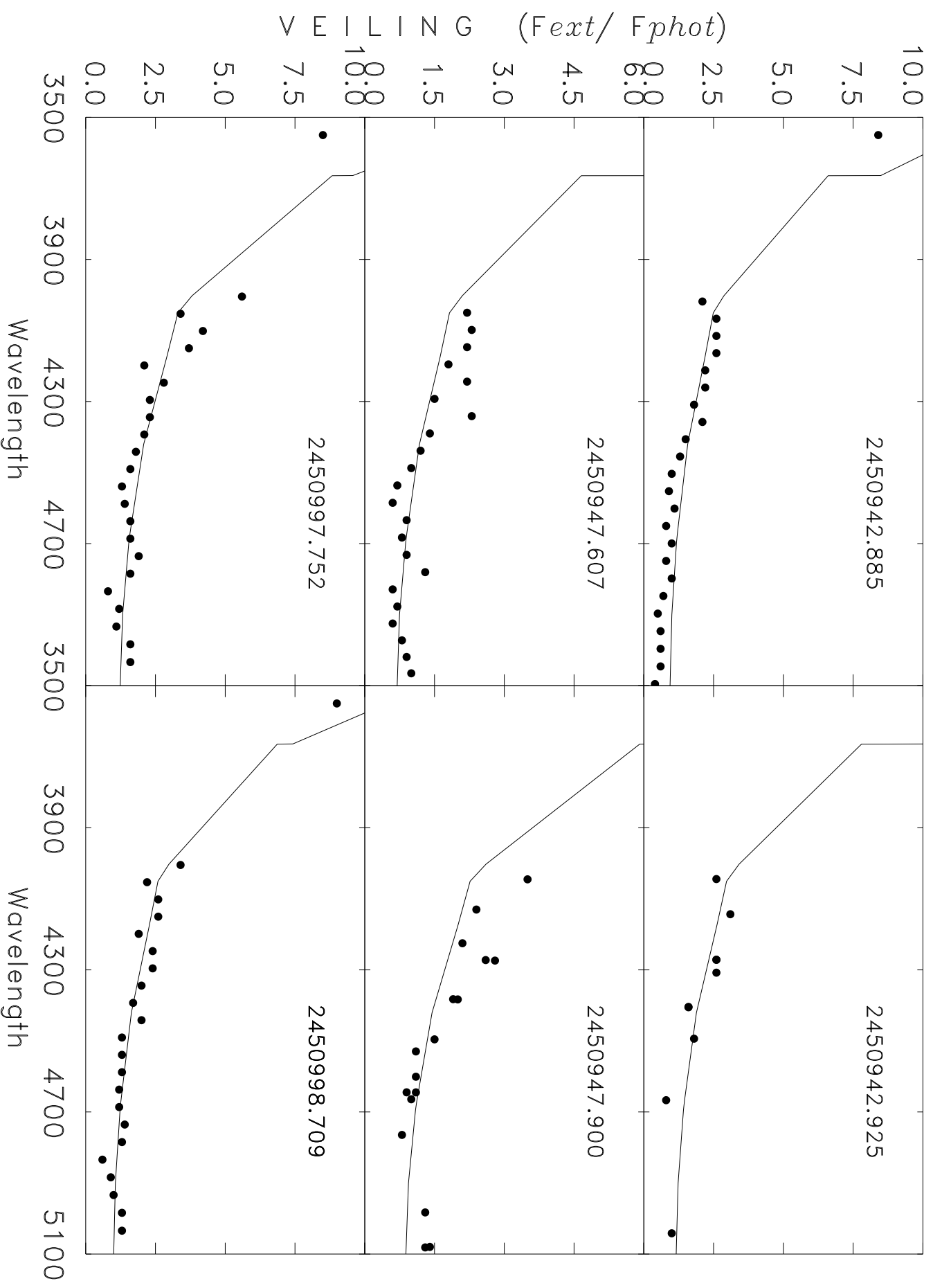


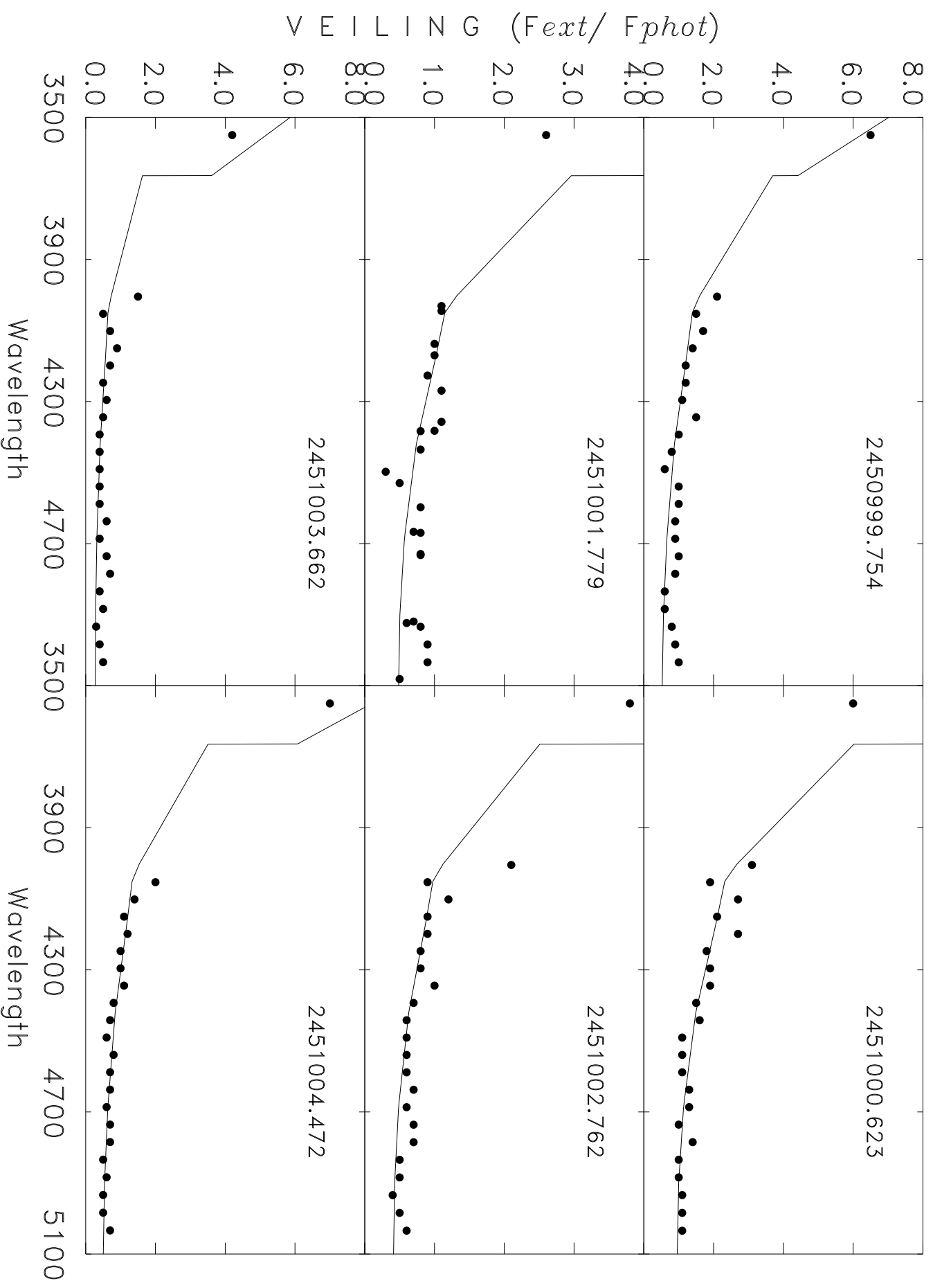
05/14/1998



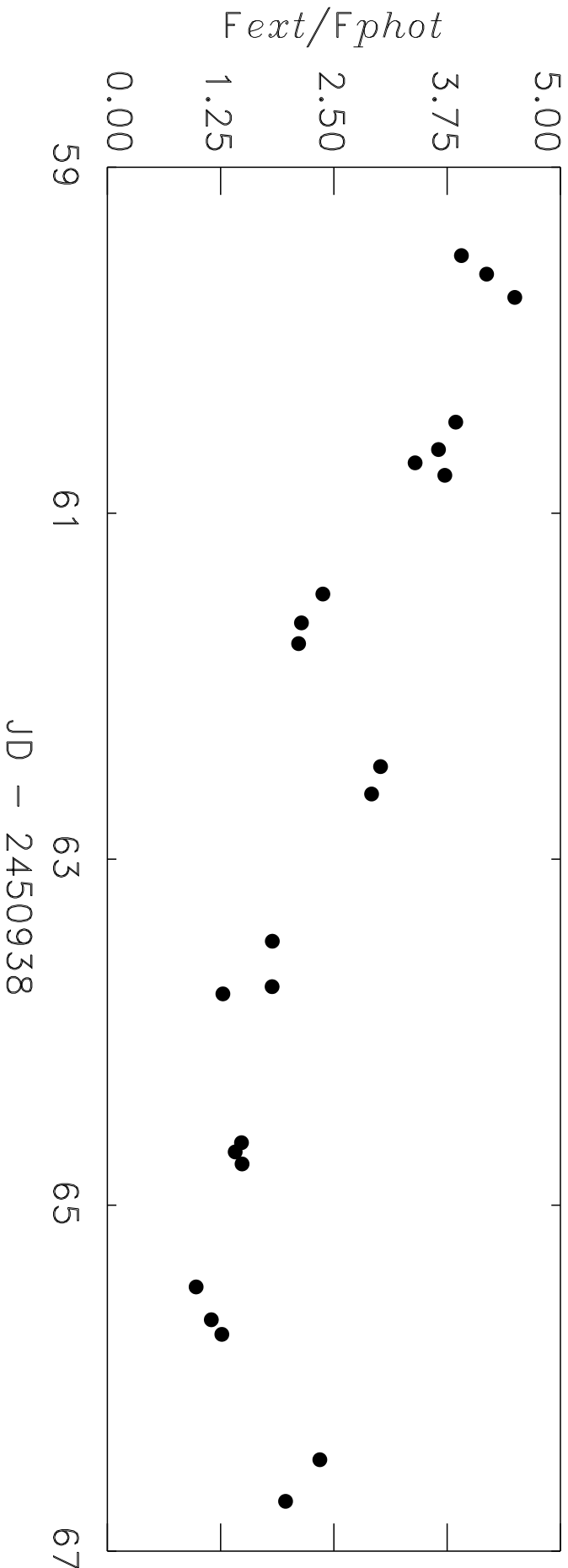
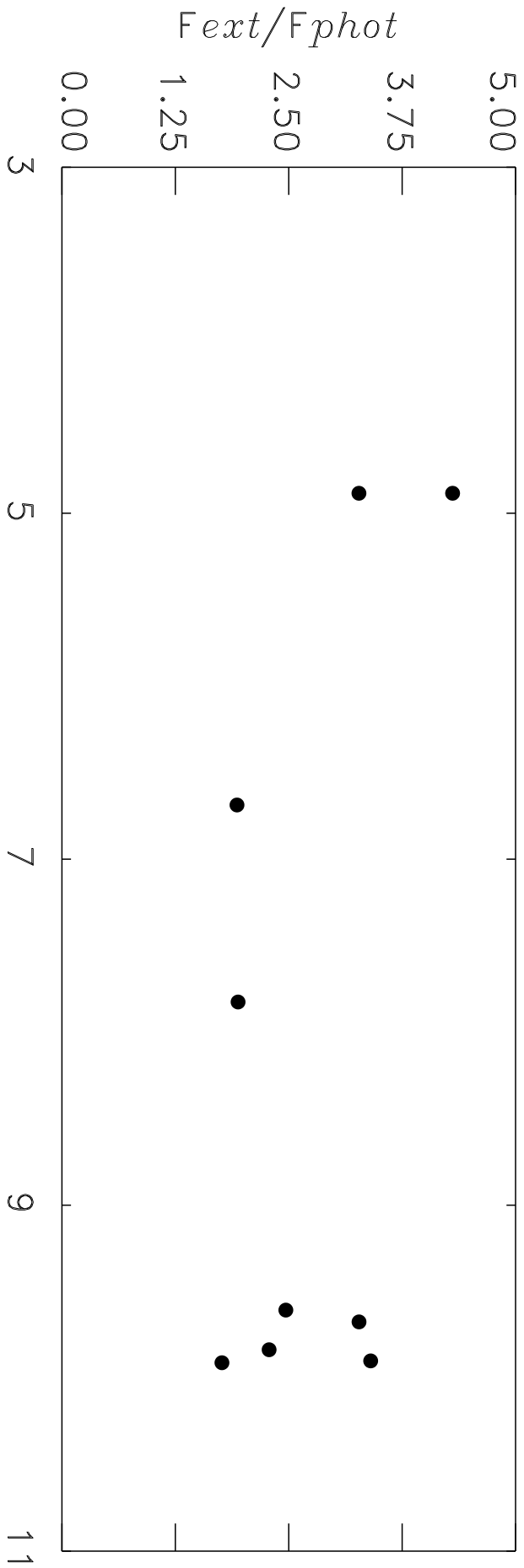




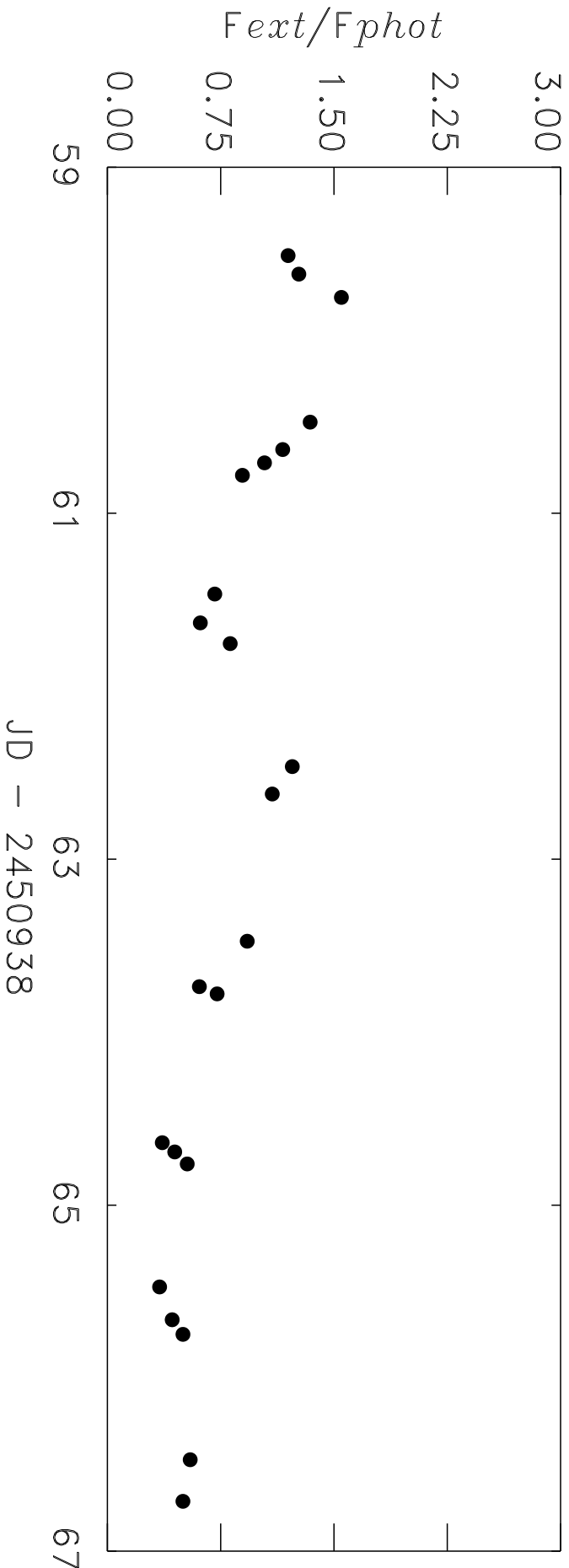
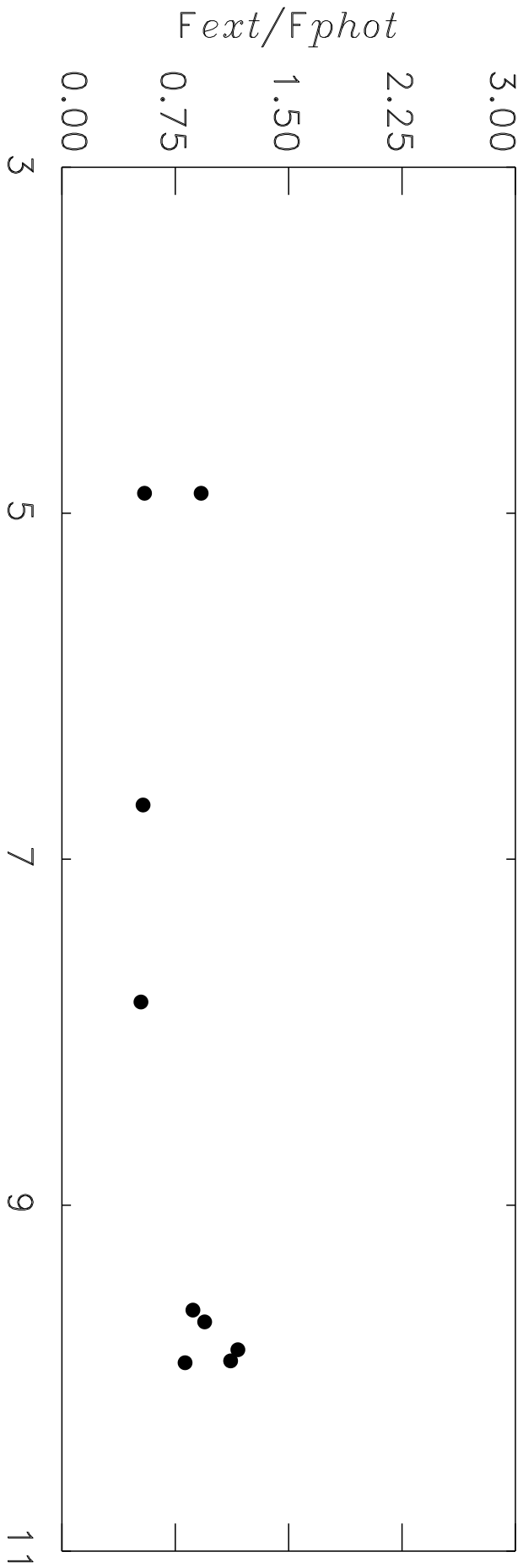




Veiling at  $\lambda = 4000\text{\AA}$



Veiling at  $\lambda = 5000\text{\AA}$





# Balmer Jump

